

Electron Correlation Effects in Attosecond Photoionization of CO₂

Andrei Kamalov,^{1,2,*} Anna L. Wang,^{1,3} Philip H. Bucksbaum,^{1,2,3} Daniel J. Haxton,⁴ and James P. Cryan^{1,5,†}

¹Stanford PULSE Institute, SLAC National Accelerator Laboratory, Menlo Park, CA, USA

²Department of Physics, Stanford University, Stanford, CA, USA

³Department of Applied Physics, Stanford University, Stanford, CA, USA

⁴KLA Corporation, Milpitas, CA, USA

⁵Linac Coherent Light Source, SLAC National Accelerator Laboratory, Menlo Park, CA, USA

(Dated: January 9, 2022)

A technique for measuring photoionization time delays with attosecond precision is combined with calculations of photoionization matrix elements to demonstrate how multi-electron dynamics affect photoionization time delays in carbon dioxide. Electron correlation is observed to affect the time delays through two mechanisms: autoionization of molecular Rydberg states and accelerated escape from a continuum shape resonance.

Photoionization is a basic quantum scattering process involving the rearrangement of degrees of freedom in the total system. In the time domain, this is described by an incoming photon wavepacket that couples to outgoing electron wavepackets (EWPs) in the final-state cation channels. The term “photoionization time delay” refers to the time required for a photoionized EWP to propagate out of the electric potential of the residual cation. It may be defined semi-classically as the extra time required to propagate a photoelectron from its birth location to a detector position, compared to some reference [1–3]. Recent advances in the production of attosecond laser pulses have enabled direct probing of these delays [4]. Combining these time delay measurements with theoretical modeling reveals the underlying quantum dynamics of the photoionization process [1–14].

Attosecond electron dynamics of ionization are necessarily violent because additional kinetic energy must be imparted to the bound electron for it to escape the Coulomb potential. The added kinetic energy may be redistributed through Coulomb and exchange scattering with other electrons, dynamically modifying this ionic potential. This is particularly important in molecular systems. Although the asymptotic state of the total system (cation plus ionized electron) is easily understood in a single-electron picture, this picture may break down when the electron has not yet escaped into the asymptotic region for detection. The modification of the ionic potential is imprinted onto the measured photoionization time delays [4], which provides direct access to the temporal evolution of electron-electron interactions. Previous measurements of photoionization time delays have made use of this effect, which has led to a deeper understanding of electron correlations in shake-up ionization [11] and atomic autoionization [14–17]. The present work combines measurements of the photoionization time delays with numerical calculations of photoionization probability amplitudes to demonstrate how multi-electron dynamics affect ionized EWPs in a molecular system.

These dynamics leave a clear signature in the measured

photoionization time delay in the vicinity of autoionizing and molecular shape resonances. The enhancement of electron correlation effects near molecular shape resonances was previously considered by Siggel *et al.* They found that the photoelectron angular distribution can be sensitive to multi-electron channel coupling phenomena [18]. The scattering angle is one of two semi-classical scattering observables; the other is time delay. The effect that electron-electron interactions would have on the interpretation of photoionization time delay measurements has yet to be considered in the literature.

Carbon dioxide (CO₂) provides a particularly striking example of multi-electron dynamics in molecular photoionization [19–22]. Straightforward close-coupling expansions require ninety-six individual cation configurations to reproduce the experimental cross section [22], far more states than are energetically available as photoionization channels. The virtual excitations of the closed cationic channels correspond to multiple-electron excitations of the molecular system, which affect the magnitude and phase of the EWPs escaping into the energetically open channels. In the present work we measure the photoionization time delays for CO₂ and demonstrate that agreement with calculated time delays is contingent upon including electron correlation effects in the calculation.

Figure 1 shows the measured photoionization time delays for the $X^2\Pi_g$, $A^2\Pi_u$, and $B^2\Sigma_u^+$ cationic states of CO₂. Details of the measurement procedure are given after a discussion of the results. In order to understand the dynamics captured in the time delay measurements, we compare these data with predicted delays calculated using an implementation [23–31] of the complex Kohn variational method [32–38] for photoionization [39–48] and electron-molecule scattering [49–58]. The photoionization time delays are calculated in two different levels of approximation and then averaged over molecular orientation and outgoing electron direction, consistent with the measurement scheme used in the experiment. The independent channel method considers the scattering in each continuum channel separately. The coupled-channel method uses fully coupled continuum states, which allows

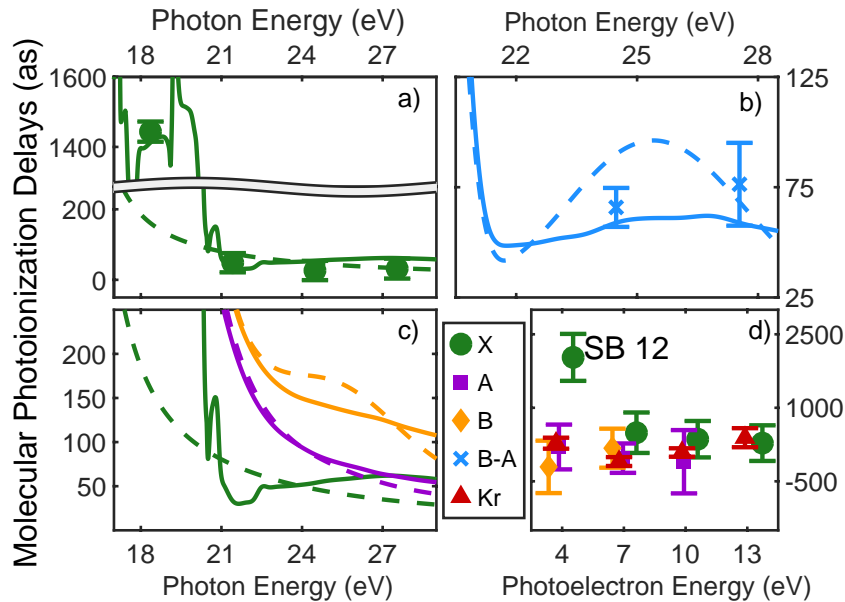


FIG. 1: Molecular photoionization time delays for the $X^2\Pi_g$ (panel a), $A^2\Pi_u$, and $B^2\Sigma_u^+$ (panel b) states of unaligned CO_2^+ . Panel c shows the finite difference approximation to the derivative of the scattering phase calculated using the complex-Kohn method and incoherently summed across all molecular orientations and electron emission angles. Calculations are done in two approximations (see text), the independent channel approximation (dashed) and coupled-channel method (solid). We compare the calculations to the measured data (panels a and b). The long delay reported for the low energy features in the X -state channel are extracted from the measurement of the sideband slope shown in panel d. In all panels, the errorbars represent the $\pm 2\sigma$ confidence level.

electrons originally produced in one ionization channel to interact with the residual ionic core to produce different final state configurations. More details of the complex-Kohn calculation are given below and in the supplemental material [59].

The independent channel calculations (dashed lines in Figure 1c) for the $X^2\Pi_g$ and $A^2\Pi_u$ channels display traditional Coulombic behavior: monotonically increasing photoionization delay with decreasing photoelectron energy [2]. The $B^2\Sigma_u^+$ channel exhibits an increased photoionization delay time around 25 eV, which is a signature [60–62] of a weak shape resonance that has been observed in the CO_2 absorption spectrum. The interchannel coupling drastically alters the predicted photoionization time delays (solid line in Figure 1c). The photoionization time delays predicted for the fully-coupled $X^2\Pi_g$ continuum become extremely long for low energy (< 20 eV) photoelectrons. This increase is caused by coupling of the $X^2\Pi_g$ continuum to Rydberg states converging to the $A^2\Pi_u$, and $B^2\Sigma_u^+$ state thresholds, i.e. autoionization. Coupling among the continuum channels also results in a decrease in the photoionization time delay in the vicinity of the shape resonance feature in the $B^2\Sigma_u^+$ -state channel. This decrease is accompanied by an increase in the photoionization time delays in the other channels.

Figures 1a and 1b compare our extracted photoionization delays to the theoretical predictions of both models and show that the measured photoionization delays are consistent with the coupled-channel theory. Moreover, there is strong disagreement with the single-channel predictions in the vicinity of the B -state shape resonance. These time-domain measurements show how electron correlation dynamics accelerate the escape of the photoelectron from the molecular potential. Electron interactions cause the EWP in the B -state continuum to transition to other available continua while it is trapped in the vicinity of the ionic core. These transitions produce photoelectrons in the $X^2\Pi_g$, $A^2\Pi_u$, and $C^2\Sigma_g$ continua with increased photoionization time delays. The couplings to the continuum channels act as additional pathways for the electron to escape the shape resonance and thus lower the photoionization delay times for the $B^2\Sigma_u^+$ state.

Figure 1a shows the measured photoionization time delays for the $X^2\Pi_g$ channel along with the single-channel and coupled channel calculations. For photoelectron energies above 20 eV, the measured delays are consistent with both the single-channel and coupled-channel predictions. Below 20 eV, the CO_2 absorption spectrum displays a series of sharp peaks associated with two Rydberg series converging to the $A^2\Pi_u$, $B^2\Sigma_u^+$ ionization thresholds [63]. The observed photoionization time delay

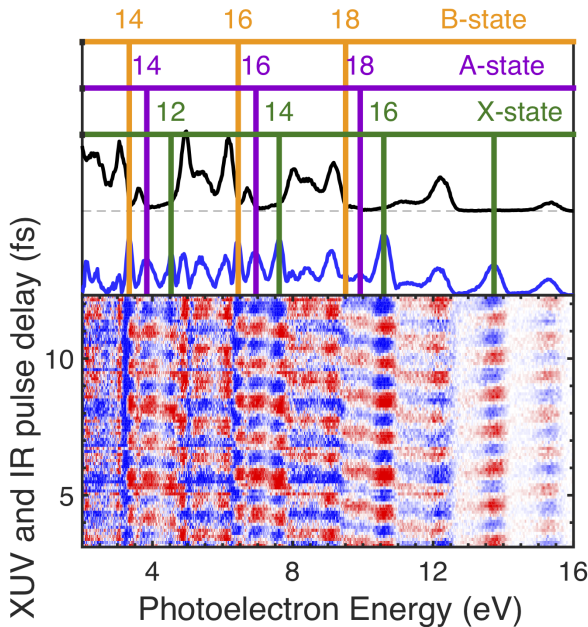


FIG. 2: Two-Color photoelectron spectrogram of CO_2 .

The upper panel shows the photoelectron spectrum recorded with only the XUV APT present. The middle panel shows the amplitude of the 2ω oscillation retrieved from the Fourier transform of the lower panel.

The lower panel shows a subset of the measured photoelectron spectrogram and demonstrates clear 2ω oscillation. All features in this panel have been assigned to either a harmonic or sideband peak of a CO_2^+ final state.

confirms the autoionizing nature of the Rydberg states, as shown on the left side of Figure 1a.

The measured photoionization time delays displayed in Figure 1 are obtained using a two-color, multi-path interference technique, which overlaps a weak infrared (IR) laser pulse, with photon energy $\hbar\omega$, and an XUV frequency comb with spectral peaks separated by $2\hbar\omega$. Such a comb appears in the time domain as an attosecond pulse train (APT), whose pulses provide the temporal resolution needed to measure EWP delays. To produce this pulse arrangement, a titanium-doped:sapphire laser (30 fs, 30 mJ, 100 Hz repetition rate) is split into three co-propagating beams: two temporally overlapped, high energy (~ 14 mJ) beams used to drive high harmonic generation (HHG) and produce the XUV APT, and a low energy (~ 1.5 mJ) beam used as an interferometric probe. All three beams are spatially displaced and focused by a common $f = 5$ m focusing optic. Near the focus, the three beams intersect in a 10 mm long gas cell filled with ~ 7 torr of argon gas. A temporal advance (~ 150 fs) is introduced in the probe beam path so that it does not disrupt the HHG process when passing through the gas

cell. The crossed-beam geometry separates the XUV and IR pulses in the far field (See SM Fig. S1) [59]. The residual drive laser light is blocked downstream from the gas cell and the probe beam passes through a $100 \mu\text{m}$ fused silica window to temporally overlap with the XUV APT. The temporal delay of the weak IR field is controlled with a piezo-electric driven delay stage. Both the XUV APT and weak IR laser pulse are focused with a B_4C coated focusing optic ($f = 10$ cm) into the interaction region of a 1.2 m magnetic bottle spectrometer [64]. The CO_2 target is introduced through a $35 \mu\text{m}$ gas needle near the interaction region. The XUV-only photoelectron spectrum of CO_2 is shown in the top panel of Fig. 2, and displays peaks spaced by twice the photon energy of the fundamental drive laser. The introduction of the weak IR field allows for two-photon absorption and produces “sideband” features between adjacent harmonic spectral features. Electron spectra are recorded as a function of XUV/IR delay, resulting in modulation of the sideband features as seen in the bottom panel of Fig. 2. This modulation occurs at twice the IR laser frequency and can be described by

$$\text{SB}_{2n}(\tau) \propto \cos[2\omega\tau + \phi_{2\omega}] \quad (1)$$

where SB_{2n} is the yield of a sideband peak as a function of τ , the relative delay between the IR and XUV pulses, and $\phi_{2\omega}$ is a phase offset in the sideband modulation that varies with sideband order ($2n$). The phase offset, $\phi_{2\omega}$, is recovered from the Fourier transform of the photoelectron spectrogram. The extracted phase offsets are shown in the supplemental material [59].

The sideband modulation is caused by interference between two different ionization pathways formed by single-photon XUV ionization by adjacent harmonics followed by subsequent absorption or emission of an IR photon [1, 65–67]. The sideband phase offset can be parsed into two contributions:

$$\phi_{2\omega} = \Delta\phi_{\text{XUV}} + \Delta\phi, \quad (2)$$

where $\Delta\phi_{\text{XUV}}$ describes the spectral phase difference between consecutive harmonics that contribute to the sideband peak, and $\Delta\phi$ describes the phase difference between the two-photon ionization pathways [1, 66]. The reconstruction of attosecond bursts by two-photon transitions (RABBITT) technique was originally developed to characterize APTs by extracting the first term in Eqn. 2 [65, 66]. Subsequent work has focused on the latter quantity in Eqn. 2 to approximate a delay for the two-photon ionization process (τ_2):

$$\frac{\Delta\phi}{2\hbar\omega} \approx \frac{\partial\phi}{\partial E} = -\frac{\tau_2}{\hbar}. \quad (3)$$

In most cases, this two-photon delay can be separated into a measurement induced (or continuum-continuum) contribution (τ_{cc}) that simply depends on the energy of

the outgoing electron ($\epsilon = E_{2n} - I_p$), and a potential-dependent term (τ_{PI}) [1, 2, 60, 68]:

$$\tau_2(E_{2n}) \approx \tau_{PI}(E_{2n}) + \tau_{cc}(\epsilon). \quad (4)$$

When the system is spherically symmetric and the ionization process is dominated by a single angular momentum partial wave, the potential dependent term can be shown to approximate the single-photon photoionization time delay [1, 68]. In this limit, the RABBITT technique has been used to investigate photoionization time delays for different continuum channels in atomic targets [2, 12, 69] as well as the relative photoionization time delay between atomic targets [8, 9]. The RABBITT technique can also be used to observe resonant processes in atomic photoionization [14–16].

The application of this interferometric technique to molecular systems is more challenging. Molecular targets often have several accessible cationic states that lead to substantial overlap of features in the photoelectron spectra (spectral congestion) [70]. Moreover, the partial-wave expansion of outgoing photoelectron wavepackets can contain a large number of coherent contributions, a challenge not typically encountered in atomic targets [71]. Nevertheless, Huppert *et al.* recently observed the effect of a molecular shape resonance on the measured photoionization time delays in N_2O^+ [62]. Vos *et al.* were able to study the stereo Wigner time delay in carbon monoxide averaged over a number of dissociative states of the CO^+ cation [72]. Due to the excellent kinetic energy resolution afforded by the magnetic bottle spectrometer, we are able to resolve the sideband oscillations for three final state channels in CO_2 (middle panel of Figure 2) and compare these results with theory predictions.

The relevant term in Eqn. 4 for theory comparison is the potential-dependent term, τ_{PI} . To extract this contribution from the measured phase offsets, we consider the phase differences between a signal (*s*) and reference (*r*) channel:

$$\begin{aligned} \Delta\tau_2(E_{2n}) &= \frac{-1}{2\omega} \left[\phi_{2\omega}^{(s)} - \phi_{2\omega}^{(r)} \right] \\ &= \Delta\tau_{PI}(E_{2n}) + \Delta\tau_{cc}(\epsilon, \epsilon'), \end{aligned} \quad (5)$$

where $\epsilon = E_{2n} - I_p^{(s)}$ and $\epsilon' = E_{2n} - I_p^{(r)}$ are the kinetic energies of the photoelectrons for the $2n^{\text{th}}$ sideband peak in the signal and reference systems, $\Delta\tau_{cc}(\epsilon, \epsilon')$ is the difference in the continuum-continuum contribution due to the mismatch in photoelectron energies and $\Delta\tau_{PI}(E_{2n})$ is the differential photoionization delay we will compare with calculations. The spectral phase variation of the XUV pulse train, $\Delta\phi_{XUV}$, has canceled out. When the relative difference between ϵ and ϵ' is small, $\Delta\tau_{cc}(\epsilon, \epsilon')$ can be calculated very accurately [68], and subtracted from Eqn. 5. For the measurements presented in Figure 1b we reference the *B*-state photoionization delay to that of the *A*-state because the two channels have similar ionization potentials ($I_{p,A} = 17.59$ eV and $I_{p,B} = 18.07$ eV).

The *X*-state channel ($I_{p,X} = 13.77$ eV, Figure 1a) is compared with a reference measurement made in krypton gas ($I_{p,Kr} = 14.00$ eV). The krypton target is well studied [69] and its photoionization delay has been calculated [7], so we remove this contribution in the differential photoionization delay.

We calculate the photoionization time delay starting from the time evolution of the EWP. In the time-domain, the EWP, $\psi(t)$, is expressed as a coherent superposition of outgoing continuum electron eigenstates ($|\psi_{\vec{k},n}^{(-)}\rangle$) with momentum \vec{k} :

$$|\psi(t)\rangle = \sum_n \int d\vec{k} c_n(\vec{k}) e^{-\frac{it}{\hbar} \left(\frac{k^2}{2} - I_{p,n} \right)} |\psi_{\vec{k},n}^{(-)}\rangle, \quad (6)$$

where n describes the final state channel with ionization potential $I_{p,n}$, and $|c_n(\vec{k})|^2$ is the photoionization probability. Additionally, we define the scattering phase $\delta_n(\vec{k}) = \text{Arg}[c_n(\vec{k})]$. The form of the outgoing electron wavefunction is described in the complex Kohn formalism and is discussed fully in the supplemental material [59]. Initially (at $t = 0$) the EWP is localized near the ionic core, but it is not stationary. The phase of each eigenstate component,

$$\Phi_n(\vec{r}, \vec{k}, t) = \text{Arg} \left[\psi_{\vec{k},n}^{(-)}(\vec{r}) \right] + \delta_n(\vec{k}) - \frac{t}{\hbar} \left(\frac{k^2}{2} - I_{p,n} \right), \quad (7)$$

evolves with time, and the wavepacket moves and disperses. The spatial location of maximum constructive interference is given by the stationary points of Eqn. 6:

$$\frac{\partial \Phi_n(\vec{r}, \vec{k}, t)}{\partial \vec{k}} = 0. \quad (8)$$

An observable delay time, τ_1 , measures the time at which an EWP of energy $E = k^2/2$ arrives at a detector some fixed position \vec{r} ($|\vec{r}| \gg 1$) from the origin, compared to the case of no scattering [1]. Combining Eqn. 7 and 8, this direction-specific value can be shown to be

$$\tau_1 = -\frac{\hbar}{k} \frac{\partial \delta_n(\vec{k})}{\partial k} = -\hbar \frac{\partial \delta_n(\vec{k})}{\partial E}. \quad (9)$$

Eqn. 9 shows the observed time delay is a direct consequence of the scattering phase, which depends on the charge dynamics that occur during photoionization. τ_1 is commonly referred to as the single-photon photoionization time delay [1, 60] or simply as the Eisenbud-Wigner-Smith delay, τ_{EWS} [73]. The measurements and calculations presented in figure 1 are related to τ_1 , but the presence of the dressing laser field, along with the experimental measurement geometry can complicate the relationship [60, 61]. The delays retrieved from the RABBITT technique, τ_{PI} , and τ_1 become identical in the special case of a spherically symmetric potential, when a single angular momentum channel dominates the photoionization process.

The ionization probability amplitude in Eqn. 6 can be calculated for weak XUV pulses from first order perturbation theory:

$$c_n(\vec{k}) = \tilde{E}_{\text{XUV}} \left(\omega = \frac{k^2 + 2I_{p,n}}{2\hbar} \right) \cdot d_n(\vec{k}) \quad (10)$$

$$d_n(\vec{k}) = \left\langle \psi_{\vec{k},n}^{(-)} \left| \hat{\mu} \cdot \vec{r} \right| \Psi_0 \right\rangle, \quad (11)$$

where $\tilde{E}_{\text{XUV}}(\omega)$ is the Fourier transform of the incident XUV pulse, $d_n(\vec{k})$ is the dipole matrix element between the outgoing and ground state (Ψ_0) wavefunctions in the length gauge, and $\hat{\mu}$ is the polarization direction in the molecular frame. The channel-resolved dipole matrix element, Eqn. 11, is computed using the complex Kohn method for photoionization [23–31, 39–48]. The calculations use explicit representations of the initial neutral state and of the final cationic states obtained with one single 11-orbital basis. This basis for the neutral and cationic states was obtained using a state-averaged multiconfiguration self-consistent-field (MCSCF) calculation performed with the *COLUMBUS* quantum chemistry program [74–78]. The orbitals obtained are a compromise between those optimized for the neutral and cationic states. The primitive basis for this MCSCF calculation was Dunning’s *aug-cc-pVDZ* basis set [79], with additional basis functions on the oxygen atom as described in the supplemental material [59]. The outgoing wavefunction, $\psi_n^{(-)}$, is expanded in a partial-wave representation (l, m), up to $l = 3$, and the dipole matrix element is calculated between these functions and the initial ground state within the approximation of separable exchange [23, 24, 28].

All meaningful partial waves are then coupled by the IR dressing field as described in Ref. [60] to determine the molecular frame (MF) two-photon photoionization time delays. These MF photoionization time delays are then averaged over both the polarization direction and outgoing electron direction to approximate the experimental conditions. This averaged quantity is what we refer to as the laboratory-frame (LF) photoionization delay as defined in Eqn. 4 and plotted in Figure 1. The single photon LF photoionization delays and two-photon MF photoionization delays for all accessible final state channels are shown in the supplemental material [59].

Observing phenomena such as autoionization, which typically have lifetimes longer than the inter-pulse spacing of our XUV pulse train (1.35 fs), requires additional considerations in the analysis. Since each attosecond burst in the train has a coherent relationship to the neighboring pulses, when time-dependent phenomena extend beyond the inter-pulse spacing, the processes induced by a single burst in the train interfere with the signal generated by the adjacent pulses. This interference leads to a burst-dependent photoemission time delay, i.e. the peak emission time is the point where all previous photoemission processes interfere constructively. Such a mod-

ulation (burst-to-burst) of the photoemission time delay leads to a variation of the phase across a sideband. This revelation is the motivation behind the development of the Rainbow RABBITT technique [14, 15]. The analysis of the slope of $\phi_{2\omega}$ across each sideband peak is shown in Figure 1d, where each channel is referenced to the krypton measurement for the $^2P_{3/2}$ continuum. The envelope of the IR-drive laser leads to small time shifts in the arrival time of each burst in the APT (referred to as harmonic chirp or femto-chirp [80]) which results in linear phase variation across a sideband peak. This contribution is removed by the krypton referencing because all measurements are made with the same APT. From the residual slope value obtained for the 12th harmonic sideband, there is a clear difference compared to any other sideband peak. Moreover, this difference is consistent with a delay of more than one complete 2ω -cycle. Instead of relying directly on the value extracted from Figure 1d, we use the slope variation to determine the number of cycles to add to the mean phase extracted from averaging the phase over the sideband peak.

These measurements and calculations demonstrate the effect of electron correlation upon time delays in photoionization of molecules. Photoionization time delays are a direct and easy-to-understand manifestation of the binding interaction that an outgoing electron experiences. We have observed two effects of electron correlation in time-domain measurements of CO₂ photoionization, via (1) a shape resonance and (2) autoionizing states, demonstrating that the inclusion of electronic correlation is important when considering resonant features in molecular photoionization with XUV light. While this seems clear for autoionizing states, which are inherently multi-channel phenomena, this result is somewhat surprising for shape resonance features which are typically considered to be single channel phenomena. For a shape resonance, we have shown that electron-electron interactions provide dynamic modifications to the effective potential that can be directly observed in all final state channels. These results highlight the need for including electron correlation when describing time-domain measurements of photoionization of molecular targets, where autoionizing states and shape resonances are omnipresent.

Molecular control (e.g. molecular alignment) techniques can be applied to isolate specific cationic states of CO₂⁺ in future experiments. Continuum-resolved molecular frame measurements will further elucidate the dependence of electron correlation on molecular orientation and electron emission angle. These experiments could be further improved by varying the XUV frequency comb spacing, thus mapping out more energy points in the differential scattering phase.

This work was supported by the AMOS program within the Chemical Sciences, Geosciences, and Biosciences Division of the Office of Basic Energy Sciences,

Office of Science, U.S. Department of Energy. Raw and analyzed data, both experimental and theoretical, along with a subset of the analysis code is available at: <https://figshare.com/account/home#/projects/63164>

* andrei.kamalov@gmail.com

† jeryan@slac.stanford.edu

- [1] J. M. Dahlström, A. L’Huillier, and A. Maquet, Introduction to attosecond delays in photoionization, *Journal of Physics B: Atomic, Molecular and Optical Physics* **45**, 183001 (2012).
- [2] K. Klünder, J. M. Dahlström, M. Gisselbrecht, T. Fordell, M. Swoboda, D. Guénot, P. Johnsson, J. Caillat, J. Mauritsson, A. Maquet, R. Taïeb, and A. L’Huillier, Probing single-photon ionization on the attosecond time scale, *Physical Review Letters* **106**, 143002 (2011).
- [3] V. V. Serov, V. L. Derbov, and T. A. Sergeeva, Interpretation of the time delay in the ionization of Coulomb and two-center systems, *Physical Review A* **87**, 063414 (2013).
- [4] R. Pazourek, S. Nagele, and J. Burgdörfer, Attosecond chronoscopy of photoemission, *Reviews of Modern Physics* **87**, 765 (2015).
- [5] M. Schultze, M. Fieß, N. Karpowicz, J. Gagnon, M. Korbman, M. Hofstetter, S. Neppl, A. L. Cavalieri, Y. Komninos, Th. Mercouris, C. A. Nicolaides, R. Pazourek, S. Nagele, J. Feist, J. Burgdörfer, A. M. Azzeer, R. Ernstorfer, R. Kienberger, U. Kleineberg, E. Goulielmakis, F. Krausz, and V. S. Yakovlev, Delay in photoemission, *Science* **328**, 1658 (2010).
- [6] D. Guénot, K. Klünder, C. L. Arnold, D. Kroon, J. M. Dahlström, M. Miranda, T. Fordell, M. Gisselbrecht, P. Johnsson, J. Mauritsson, E. Lindroth, A. Maquet, R. Taïeb, A. L’Huillier, and A. S. Kheifets, Photoemission-time-delay measurements and calculations close to the $3s$ -ionization-cross-section minimum in Ar, *Physical Review A* **85**, 053424 (2012).
- [7] A. S. Kheifets, Time delay in valence-shell photoionization of noble-gas atoms, *Physical Review A* **87**, 063404 (2013).
- [8] D. Guénot, D. Kroon, E. Balogh, E. W. Larsen, M. Kotur, M. Miranda, T. Fordell, P. Johnsson, J. Mauritsson, M. Gisselbrecht, K. Varjú, C. L. Arnold, T. Carette, A. S. Kheifets, E. Lindroth, A. L’Huillier, and J. M. Dahlström, Measurements of relative photoemission time delays in noble gas atoms, *Journal of Physics B: Atomic, Molecular and Optical Physics* **47**, 245602 (2014).
- [9] C. Palatchi, J. M. Dahlström, A. S. Kheifets, I. A. Ivanov, D. M. Canaday, P. Agostini, and L. F. DiMauro, Atomic delay in helium, neon, argon and krypton, *Journal of Physics B: Atomic, Molecular and Optical Physics* **47**, 245003 (2014).
- [10] M. Sabbar, S. Heuser, R. Boge, M. Lucchini, T. Carette, E. Lindroth, L. Gallmann, C. Cirelli, and U. Keller, Resonance effects in photoemission time delays, *Physical Review Letters* **115**, 133001 (2015).
- [11] M. Ossiander, F. Siegrist, V. Shirvanyan, R. Pazourek, A. Sommer, T. Latka, A. Guggenmos, S. Nagele, J. Feist, J. Burgdörfer, R. Kienberger, and M. Schultze, Attosecond correlation dynamics, *Nature Physics* **13**, 280 (2017).
- [12] M. Isinger, R. J. Squibb, D. Busto, S. Zhong, A. Harth, D. Kroon, S. Nandi, C. L. Arnold, M. Miranda, J. M. Dahlström, E. Lindroth, R. Feifel, M. Gisselbrecht, and A. L’Huillier, Photoionization in the time and frequency domain, *Science* **358**, 893 (2017).
- [13] D. Kiesewetter, R. R. Jones, A. Camper, S. B. Schoun, P. Agostini, and L. F. DiMauro, Probing electronic binding potentials with attosecond photoelectron wavepackets, *Nature Physics* **14**, 68 (2017).
- [14] D. Busto, L. Barreau, M. Isinger, M. Turconi, C. Alexandridi, A. Harth, S. Zhong, R. J. Squibb, D. Kroon, S. Plogmaker, M. Miranda, Á Jiménez-Galán, L. Argenti, C. L. Arnold, R. Feifel, F. Martín, M. Gisselbrecht, A. L’Huillier, and P. Salières, Time-frequency representation of autoionization dynamics in helium, *Journal of Physics B: Atomic, Molecular and Optical Physics* **51**, 044002 (2018).
- [15] V. Gruson, L. Barreau, Á Jiménez-Galan, F. Risoud, J. Caillat, A. Maquet, B. Carré, F. Lepetit, J.-F. Hergott, T. Ruchon, L. Argenti, R. Taïeb, F. Martín, and P. Salières, Attosecond dynamics through a Fano resonance: Monitoring the birth of a photoelectron, *Science* **354**, 734 (2016).
- [16] M. Kotur, D. Guénot, Á Jiménez-Galán, D. Kroon, E. W. Larsen, M. Louisy, S. Bengtsson, M. Miranda, J. Mauritsson, C. L. Arnold, S. E. Canton, M. Gisselbrecht, T. Carette, J. M. Dahlström, E. Lindroth, A. Maquet, L. Argenti, F. Martín, and A. L’Huillier, Spectral phase measurement of a Fano resonance using tunable attosecond pulses, *Nature Communications* **7**, 10566 (2016).
- [17] C. Cirelli, C. Marante, S. Heuser, C. L. M. Petersson, Á. Jiménez Galán, L. Argenti, S. Zhong, D. Busto, M. Isinger, S. Nandi, S. Maclot, L. Rading, P. Johnsson, M. Gisselbrecht, M. Lucchini, L. Gallmann, J. M. Dahlström, E. Lindroth, A. L’Huillier, F. Martín, and U. Keller, Anisotropic photoemission time delays close to a Fano resonance, *Nature Communications* **9**, 955 (2018).
- [18] M. R. F. Siggel, J. B. West, M. A. Hayes, A. C. Parr, J. L. Dehmer, and I. Iga, Shape-resonance-enhanced continuum-continuum coupling in photoionization of CO₂, *The Journal of Chemical Physics* **99**, 1556 (1993).
- [19] R. R. Lucchese and V. McKoy, Studies of differential and total photoionization cross sections of carbon dioxide, *Physical Review A* **26**, 1406 (1982).
- [20] R. R. Lucchese, Effects of interchannel coupling on the photoionization cross sections of carbon dioxide, *The Journal of Chemical Physics* **92**, 4203 (1990).
- [21] R. R. Lucchese and V. McKoy, Comparative studies of a shape-resonant feature in the photoionization of CO₂, *The Journal of Physical Chemistry* **85**, 2166 (1981).
- [22] A. G. Harvey, D. S. Brambila, F. Morales, and O. Smirnova, An R-matrix approach to electron-photon-molecule collisions: photoelectron angular distributions from aligned molecules, *Journal of Physics B: Atomic, Molecular and Optical Physics* **47**, 215005 (2014).
- [23] T. N. Rescigno and A. E. Orel, Separable approximation for exchange interactions in electron-molecule scattering, *Physical Review A* **24**, 1267 (1981).
- [24] T. N. Rescigno and B. I. Schneider, Disappearance of continuum exchange integrals from algebraic variational calculations of electron scattering, *Physical Review A* **37**, 1044(R) (1988).

- [25] B. I. Schneider and T. N. Rescigno, Complex Kohn variational method: Application to low-energy electron-molecule collisions, *Physical Review A* **37**, 3749 (1988).
- [26] A. E. Orel and T. N. Rescigno, Variational expressions for first-order properties involving continuum wave functions, *Physical Review A* **41**, 1695 (1990).
- [27] T. N. Rescigno and A. E. Orel, Continuum basis functions in the complex Kohn variational method, *Physical Review A* **43**, 1625 (1991).
- [28] C. W. McCurdy and T. N. Rescigno, Beyond the primitive separable exchange approximation in electron-molecule scattering, *Physical Review A* **46**, 255 (1992).
- [29] T. N. Rescigno, A. E. Orel, and C. W. McCurdy, Algebraic variational approach to atomic and molecular photoionization cross sections: Removing the energy dependence from the basis, *Physical Review A* **55**, 342 (1997).
- [30] T. N. Rescigno and C. W. McCurdy, Improvements to the “standard” complex Kohn variational method: Towards the development of an “R-matrix theory without a box”, in *Novel Aspects of Electron-Molecule Collisions*, edited by K. H. Becker (World Scientific Publishing, Singapore, 1998) 325.
- [31] C. W. McCurdy, T. N. Rescigno, W. A. Isaacs, and D. E. Manolopoulos, Calculation of scattering amplitudes as continuous functions of energy: R-matrix theory without a box, *Physical Review A* **57**, 3511 (1998).
- [32] W. Kohn, Variational methods in nuclear collision problems, *Physical Review* **74**, 1763 (1948).
- [33] R. K. Nesbet, Analysis of the Harris variational method in scattering theory, *Physical Review* **175**, 134 (1968).
- [34] R. K. Nesbet, Anomaly-free variational method for inelastic scattering, *Physical Review* **179**, 60 (1969).
- [35] *Electron-molecule and photon-molecule collisions*, edited by T. N. Rescigno, V. McKoy, and B. I. Schneider, (Plenum, New York, NY, 1979).
- [36] C. W. McCurdy, T. N. Rescigno, and B. I. Schneider, Interrelation between variational principles for scattering amplitudes and generalized R-matrix theory, *Physical Review A* **36**, 2061 (1987).
- [37] J. Z. H. Zhang, S. I. Chu, and W. H. Miller, Quantum scattering via the S-matrix version of the Kohn variational principle, *The Journal of Chemical Physics* **88**, 6233 (1988).
- [38] T. N. Rescigno, C. W. McCurdy, A. E. Orel, and B. H. Lengsfeld, III, The complex Kohn variational method, in *Computational methods for electron-molecule collisions*, edited by W. M. Huo and F. A. Gianturco (Springer US, Boston, MA, 1995) 1.
- [39] T. N. Rescigno, B. H. Lengsfeld, and A. E. Orel, Interchannel coupling and ground state correlation effects in the photoionization of CO, *The Journal of Chemical Physics* **99**, 5097 (1993).
- [40] A. E. Orel and T. N. Rescigno, Photoionization of ammonia, *Chemical Physics Letters* **269**, 222 (1997).
- [41] S. Miyabe, C. W. McCurdy, A. E. Orel, and T. N. Rescigno, Theoretical study of asymmetric molecular-frame photoelectron angular distributions for C 1s photoejection from CO₂, *Physical Review A* **79**, 053401 (2009).
- [42] H. Sann, T. Jahnke, T. Havermeier, K. Kreidi, C. Stuck, M. Meckel, M. S. Schöffler, N. Neumann, R. Wallauer, S. Voss, A. Czasch, O. Jagutzki, Th. Weber, H. Schmidt-Böcking, S. Miyabe, D. J. Haxton, A.E. Orel, T. N. Rescigno, and R. Dörner, Electron diffraction self-imaging of molecular fragmentation in two-step double ionization of water, *Physical Review Letters* **106**, 133001 (2011).
- [43] J. B. Williams, C. S. Trevisan, M. S. Schöffler, T. Jahnke, I. Bocharova, H. Kim, B. Ulrich, R. Wallauer, F. Sturm, T. N. Rescigno, A. Belkacem, R. Dörner, Th. Weber, C. W. McCurdy, and A. L. Landers, Imaging polyatomic molecules in three dimensions using molecular frame photoelectron angular distributions, *Physical Review Letters* **108**, 233002 (2012).
- [44] N. Douguet, T. N. Rescigno, and A. E. Orel, Time-resolved molecular-frame photoelectron angular distributions: Snapshots of acetylene-vinylidene cationic isomerization, *Physical Review A* **86**, 013425 (2012).
- [45] S. Marggi Poullain, C. Elkharrat, W. B. Li, K. Veyrinas, J. C. Houver, C. Cornaggia, T. N. Rescigno, R. R. Lucchese, and D. Dowek, Recoil frame photoemission in multiphoton ionization of small polyatomic molecules: photodynamics of NO₂ probed by 400 nm fs pulses, *Journal of Physics B: Atomic, Molecular and Optical Physics* **47**, 124024 (2014).
- [46] S. Fonseca dos Santos, N. Douguet, A. E. Orel, and T. N. Rescigno, Ligand effects in carbon-K-shell photoionization, *Physical Review A* **91**, 023408 (2015).
- [47] C. W. McCurdy, T. N. Rescigno, C. S. Trevisan, R. R. Lucchese, B. Gaire, A. Menssen, M. S. Schöffler, A. Gattton, J. Neff, P. M. Stammer, J. Rist, S. Eckart, B. Berry, T. Severt, J. Sartor, A. Moradmand, T. Jahnke, A. L. Landers, J. B. Williams, I. Ben-Itzhak, R. Dörner, A. Belkacem, and Th. Weber, Unambiguous observation of F-atom core-hole localization in CF₄ through body-frame photoelectron angular distributions, *Physical Review A* **95**, 011401(R) (2017).
- [48] E. G. Champenois, L. Greenman, N. Shivaram, J. P. Cryan, K. A. Larsen, T. N. Rescigno, C. W. McCurdy, A. Belkacem, and D. S. Slaughter, Ultrafast photodissociation dynamics and nonadiabatic coupling between excited electronic states of methanol probed by time-resolved photoelectron spectroscopy, *The Journal of Chemical Physics* **150**, 114301 (2019).
- [49] A. U. Hazi, A. E. Orel, and T. N. Rescigno, *Ab initio* study of dissociative attachment of low-energy electrons to F₂, *Physical Review Letters* **46**, 918 (1981).
- [50] T. N. Rescigno, C. W. McCurdy, and B. I. Schneider, Accurate *ab initio* treatment of low-energy electron collisions with polyatomic molecules: Resonant electron-formaldehyde scattering, *Physical Review Letters* **63**, 248 (1989).
- [51] B. I. Schneider, T. N. Rescigno, B. H. Lengsfeld, III, and C. W. McCurdy, Accurate *ab initio* treatment of low-energy electron collisions with ethylene, *Physical Review Letters* **66**, 2728 (1991).
- [52] B. H. Lengsfeld, III and T. N. Rescigno, Electron-molecule close coupling with correlated target wave functions: Application to impact dissociation of F₂, *Physical Review A* **44**, 2913 (1991).
- [53] T. J. Gil, C. W. McCurdy, T. N. Rescigno, and B. H. Lengsfeld, III, Polarization and correlation effects in elastic electron-Li₂ scattering, *Physical Review A* **47**, 255 (1993).
- [54] T. N. Rescigno, D. A. Byrum, W. A. Isaacs, and C. W. McCurdy, Theoretical studies of low-energy electron-CO₂ scattering: Total, elastic, and differential cross sections, *Physical Review A* **60**, 2186 (1999).

- [55] T. N. Rescigno, C. S. Trevisan, and A. E. Orel, Dynamics of low-energy electron attachment to formic acid, *Physical Review Letters* **96**, 213201 (2006).
- [56] H. Adaniya, B. Rudek, T. Osipov, D. J. Haxton, T. Weber, T. N. Rescigno, C. W. McCurdy, and A. Belkacem, Imaging the molecular dynamics of dissociative electron attachment to water, *Physical Review Letters* **103**, 233201 (2009).
- [57] D. S. Slaughter, A. Belkacem, C. W. McCurdy, T. N. Rescigno, and D. J. Haxton, Ion-momentum imaging of dissociative attachment of electrons to molecules, *Journal of Physics B: Atomic, Molecular and Optical Physics* **49**, 222001 (2016).
- [58] T. N. Rescigno, C. S. Trevisan, A. E. Orel, D. S. Slaughter, H. Adaniya, A. Belkacem, Marvin Weyland, Alexander Dorn, and C. W. McCurdy, Dynamics of dissociative electron attachment to ammonia, *Physical Review A* **93**, 052704 (2016).
- [59] See Supplemental Material at [URL will be inserted by publisher] for a more detailed description of the data and theory analysis
- [60] D. Baykusheva and H. J. Wörner, Theory of attosecond delays in molecular photoionization, *The Journal of Chemical Physics* **146**, 124306 (2017).
- [61] P. Hockett, E. Frumker, D. M. Villeneuve, and P. B. Corkum, Time delay in molecular photoionization, *Journal of Physics B: Atomic, Molecular and Optical Physics* **49**, 095602 (2016).
- [62] M. Huppert, I. Jordan, D. Baykusheva, A. von Conta, and H. J. Wörner, Attosecond delays in molecular photoionization, *Physical Review Letters* **117**, 093001 (2016).
- [63] W. F. Chan, G. Cooper, and C. E. Brion, The electronic spectrum of carbon dioxide. Discrete and continuum photoabsorption oscillator strengths (6-203 eV), *Chemical Physics* **178**, 401 (1993).
- [64] M. Mücke, M. Braune, S. Barth, M. Förstel, T. Lischke, V. Ulrich, T. Arion, U. Becker, A. Bradshaw, and U. Hergenhahn, A hitherto unrecognized source of low-energy electrons in water, *Nature Physics* **6**, 143 (2010).
- [65] P. M. Paul, E. S. Toma, P. Breger, G. Mullot, F. Augé, Ph. Balcou, H. G. Muller, and P. Agostini, Observation of a train of attosecond pulses from high harmonic generation, *Science* **292**, 1689 (2001).
- [66] H. G. Muller, Reconstruction of attosecond harmonic beating by interference of two-photon transitions, *Applied Physics B* **74(Suppl 1)**, s17 (2002).
- [67] Y. Mairesse and F. Quéré, Frequency-resolved optical gating for complete reconstruction of attosecond bursts, *Physical Review A* **71**, 011401(R) (2005).
- [68] J. M. Dahlström, D. Guénot, K. Klünder, M. Gisselbrecht, J. Mauritsson, A. L’Huillier, A. Maquet, and R. Taïeb, Theory of attosecond delays in laser-assisted photoionization, *Chemical Physics* **414**, 53 (2013).
- [69] I. Jordan, M. Huppert, S. Pabst, A. S. Kheifets, D. Baykusheva, and H. J. Wörner, Spin-orbit delays in photoemission, *Physical Review A* **95**, 013404 (2017).
- [70] I. Jordan and H. J. Wörner, Extracting attosecond delays from spectrally overlapping interferograms, *Journal of Optics* **20**, 024013 (2018).
- [71] U. Fano, Propensity rules: An analytical approach, *Physical Review A* **32**, 617 (1985).
- [72] J. Vos, L. Cattaneo, S. Patchkovskii, T. Zimmermann, C. Cirelli, M. Lucchini, A. Kheifets, A. S. Landsman, and U. Keller, Orientation-dependent stereo Wigner time delay and electron localization in a small molecule, *Science* **360**, 1326 (2018).
- [73] E. P. Wigner, Lower Limit for the Energy Derivative of the Scattering Phase Shift, *Physical Review* **98**, 145 (1955).
- [74] H. Lischka, R. Shepard, F. B. Brown, and I. Shavitt, New implementation of the graphical unitary group approach for multireference direct configuration interaction calculations, *International Journal of Quantum Chemistry* **20**, 91 (1981).
- [75] R. Shepard, I. Shavitt, R. M. Pitzer, D. C. Comeau, M. Pepper, H. Lischka, P. G. Szalay, R. Ahlrichs, F. B. Brown, and J.-G. Zhao, A progress report on the status of the *COLUMBUS* MRCI program system, *International Journal of Quantum Chemistry* **34**, 149 (1988).
- [76] H. Lischka, R. Shepard, R. M. Pitzer, I. Shavitt, M. Dallos, T. Müller, P. G. Szalay, M. Seth, G. S. Kedziora, S. Yabushita, and Z. Zhang, High-level multireference methods in the quantum-chemistry program system *COLUMBUS*: Analytic MR-CISD and MR-AQCC gradients and MR-AQCC-LRT for excited states, GUGA spin-orbit CI and parallel CI density, *Physical Chemistry Chemical Physics* **3**, 664 (2001).
- [77] H. Lischka, T. Müller, P. G. Szalay, I. Shavitt, R. M. Pitzer, and R. Shepard, *COLUMBUS*-a program system for advanced multireference theory calculations, *Wiley Interdisciplinary Reviews: Computational Molecular Science* **1**, 191 (2011).
- [78] H. Lischka, R. Shepard, I. Shavitt, R. M. Pitzer, M. Dallos, Th. Müller, P. G. Szalay, F. B. Brown, R. Ahlrichs, H. J. Böhm, A. Chang, D. C. Comeau, R. Gdanitz, H. Dachsel, C. Ehrhardt, M. Ernzerhof, P. Höchtel, S. Irle, G. Kedziora, T. Kovar, V. Parasuk, M. J. M. Pepper, P. Scharf, H. Schiffer, M. Schindler, M. Schüler, M. Seth, E. A. Stahlberg, J.-G. Zhao, S. Yabushita, Z. Zhang, M. Barbatti, S. Matsika, M. Schuurmann, D. R. Yarkony, S. R. Brozell, E. V. Beck, J.-P. Blaudeau, M. Ruckebauer, B. Sellner, F. Plasser, and J. J. Szymczak, *Columbus*, an ab initio electronic structure program (2012), release 7.0.
- [79] T. H. Dunning, Jr., Gaussian basis sets for use in correlated molecular calculations. I. The atoms boron through neon and hydrogen, *The Journal of Chemical Physics* **90**, 1007 (1989).
- [80] K. Varjú, Y. Mairesse, B. Carré, M. B. Gaarde, P. Johnsson, S. Kazamias, R. López-Martens, J. Mauritsson, K. J. Schafer, Ph. Balcou, A. L’huillier, and P. Salières, Frequency chirp of harmonic and attosecond pulses, *Journal of Modern Optics* **52**, 379 (2005).

Supplementary Material for “Electron Correlation Effects in Attosecond Photoionization of CO₂”

Andrei Kamalov^{1,2}, Anna L. Wang^{1,3}, Philip H.

Bucksbaum^{1,2,3}, Daniel J. Haxton⁴, and James P. Cryan^{1,5}

¹*Stanford PULSE Institute, SLAC National Accelerator Laboratory, Menlo Park, CA, USA*

²*Department of Physics, Stanford University, Stanford, CA, USA*

³*Department of Applied Physics, Stanford University, Stanford, CA, USA*

⁴*KLA Corporation, Milpitas, CA, USA and*

⁵*Linac Coherent Light Source, SLAC National
Accelerator Laboratory, Menlo Park, CA, USA*

(Dated: January 9, 2022)

CONTENTS

I. Experimental Setup	2
A. Optical Laser	2
B. Photoelectron Spectrometer	4
II. Data Analysis	4
A. Extracting the 2ω signal	4
B. Delay-stage drift compensation	5
C. Comparative RABBITT	7
III. Theory	8
A. Channel Coupling in Two-Color Photoionization	8
B. Complex Kohn Photoionization Calculations	12
C. Molecular Photoionization Delays	14
D. Effects of Angular Averaging	15
References	18

I. EXPERIMENTAL SETUP

A. Optical Laser

The general layout of the optical system is described in the main text. Here we supplement the previous description with some additional details. The three beams used in the experiment are created by a set of nested interferometers, that produce three spatially separated beams, as shown in Fig. S1. We monitor the stability of the pump beam interferometer by measuring the fringe stability in the focused beams. The pulse compressor and nested interferometers reside within a low-vacuum chamber (180 Torr) that is back-filled with helium. The helium atmosphere maintains thermal equilibrium for optical components while minimizing chromatic dispersion and nonlinear propagation effects. All three beams are focused with a common $f = 5$ m focusing optic. After which, all three beams pass through a thin glass window which separates the low-vacuum chamber from the remainder of the beamline, which is maintained at high vacuum. As shown in Fig. S1 all three beams

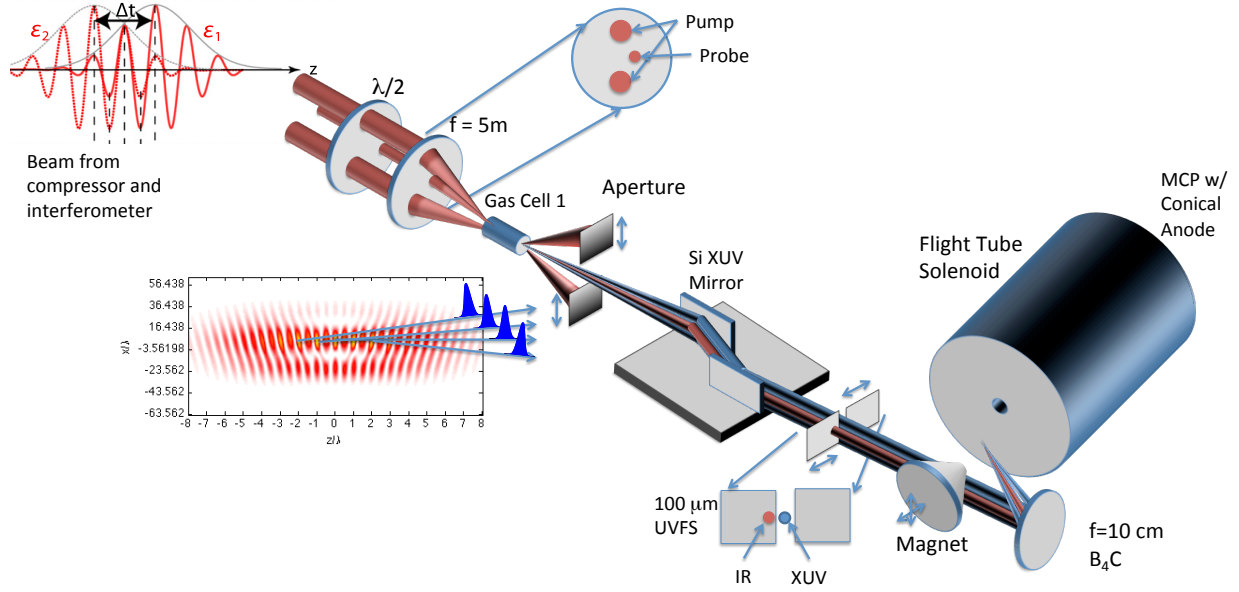


FIG. S1: Experimental Layout showing crossed beam geometry

intersect near the focus, inside of a ~ 1 cm gas cell filled with ~ 7 torr of argon gas. The sides of the gas cell consist of replaceable thin copper shims which are laser-drilled through to produce apertures the size of the IR beams.

The XUV pulse train, produced by the overlapping pump beams, propagates between the two pump beams and is spatially filtered from the IR pump beams. A thin glass plate is introduced to temporally retard the probe field by ~ 150 fs while simultaneously retarding background IR by the same value (see Fig. S1). This temporally overlaps the XUV APT with the probing laser field.

As shown in Fig. S1 the XUV and IR-probe beams are back-focused with a B_4C coated 0° focusing optic ($f = 10$ cm). The B_4C coating reflects up to the 19th harmonic (29 eV) of the HHG drive laser. The focus spot is vertically offset such that the focus is spatially separated from the incoming XUV beam path. A $35 \mu\text{m}$ effusive gas needle is positioned just above the focus spot. A 1.22 m magnetic bottle type time of flight (ToF) detector is used to collect photoelectrons produced by the focused XUV beam. The gas needle and permanent magnet were positioned outside of the true focus of the IR-field to avoid the Gouy phase shift.

B. Photoelectron Spectrometer

The magnetic bottle solenoid was set to have a uniform magnetic field of strength $\sim 300 \mu\text{T}$ and used a permanent magnet with peak field $\sim 1 \text{ T}$. A soft iron cone was attached to the magnet, and the cone tip was positioned near the interaction region. The base pressure for the chamber is $4 \times 10^{-9} \text{ Torr}$, and the experiments were performed with a chamber pressure close to $2 \times 10^{-7} \text{ Torr}$. A multi-channel plate (MCP) detector with a conical anode is positioned at the end of the solenoid. The anode signal is amplified and digitized by a computer mounted digitizer card with 1 ns precision. The digitized trace is discriminated, and each recorded time-of-flight (ToF) is saved to disk. The resolution of the photoelectron spectrum was used to optimize the positions of the gas needle, the permanent magnet, the magnetic bottle's solenoid orientation, and solenoid current.

II. DATA ANALYSIS

XUV/IR delay scans were performed for the target, CO_2 , and reference, Kr, in alternate fashion. We scan the XUV/IR delay randomly over 223 unique delay values with 120 as spacing. An additional delay point, where the XUV and IR fields do not temporally overlap, is recorded as an additional background. After acquiring the photoelectron spectrum for 1400 laser shots at each delay point ($\sim 40 \text{ min.}$), the data is saved to disk, and the gas target is changed. The data presented in Fig. 1 is the result of 51 independent measurement scans. The reference gas data enables photoelectron energy calibration, delay-stage drift compensation, and provides a reference signal for the $X^2\Pi_g$ state data.

A. Extracting the 2ω signal

Fig. S2 shows the delay-dependent photoelectron spectra collected for both target gases. The figures show that a clear beating signal is observed in the photoelectron spectra as the time delay is varied. The sideband phase offset from Eqn. 1 of the main text is isolated by Fourier transforming the photoelectron spectrogram, and extracting the phase of the 2ω component. This phase is then averaged over a 0.1 eV (0.3 eV) wide window centered on

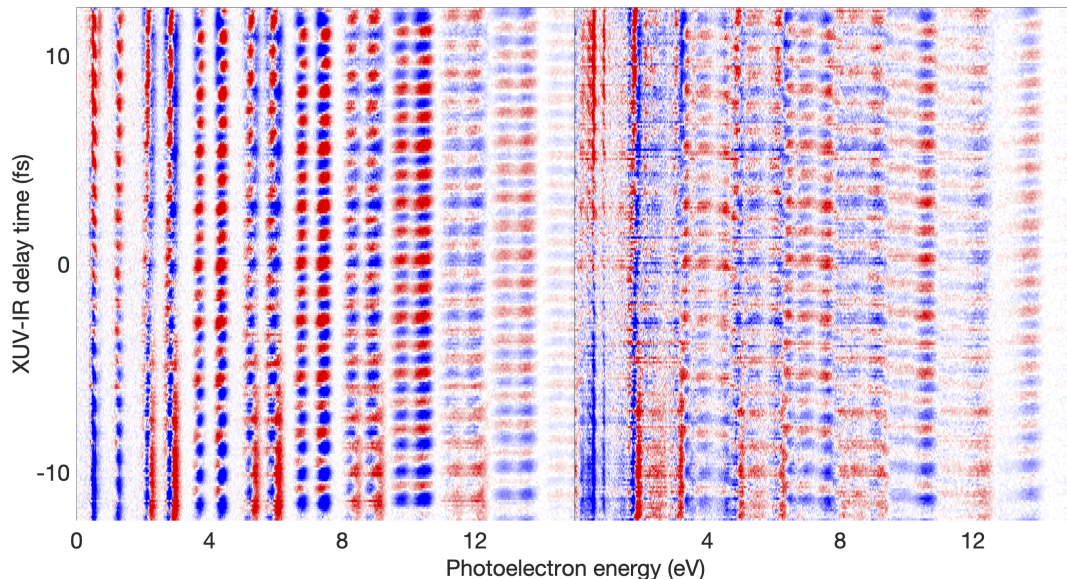


FIG. S2: Spectrographs for Kr (left) and CO_2 (right). Photoelectron spectra are collected at many different time delay values between the XUV and IR fields. As the fields are varied, there is a clear beating in the amplitude of the photoelectronic signal. The spectrographs shown here are mean-subtracted for visual clarity.

each sideband peak of CO_2 (Kr), weighted by the Fourier Amplitude (spectral integration).

$$\text{Arg} \left[\int A_{2\omega}(E) e^{i\phi_{2\omega}(E)} dE \right] \quad (1)$$

Spectral fitting was performed to test whether the $A^2\Pi_u$ and $B^2\Sigma_u^+$ signals were affected by the $C^2\Sigma_g^+$ state. The spectral fitting results matched the values returned from spectral integration within confidence intervals.

B. Delay-stage drift compensation

Comparing the phase offset across the 51 independent measurement scans, requires precise knowledge of any drifts in the XUV/IR laser delay. We use the interleaved measurements of the krypton reference to track the long-term drift of the delay stage. For each Kr scan, the extracted sideband offset from spectral integration is combined into a weighted average,

$$\Phi = \sum_{n=SB} \text{Arg}[e^{i\phi_{2\omega}(E_n)}], \quad (2)$$

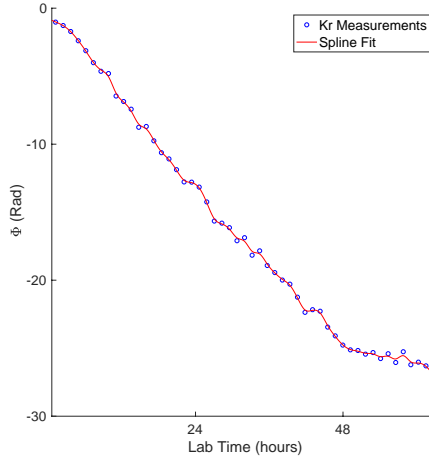


FIG. S3: Variation of Φ , the delay-stage drift metric, throughout the duration of the run. Measurements (blue) are made during Kr scans. A spline fit (red) is used to estimate delay-stage drift values during CO_2 scans performed between adjacent Kr scans.

which is used to track the delay-stage drift across the length of the run. Figure S3 shows the evolution of Φ throughout the duration of the experimental run. A smoothing spline is fit to the experimental values of Φ and is used to interpolate the value of Φ at each CO_2 scan. We subtract the interpolated value of Φ from each CO_2 scan to account for delay-stage drift. This procedure accounts for most, but not all of the delay-stage artifact.

The residual artifacts are easily seen in Figure S4, which shows the results from five chronological CO_2 measurements following the referencing feature described above. Figure S4a shows that the individual experiments reproduce similar trend lines across the sampled photoelectron energies, however, the individual experiments still exhibit a systematic phase shift between experiments. For each CO_2 dataset we again calculate the weighted sideband offset, Eqn.2, the distribution of these offsets is shown in Figure S4b. Removing this weighted offset yields Figure S4c, which shows a greatly reduced variation in the measured phase offset.

We interpret this behavior as a systematic uncertainty in the zero-phase measurement along with a random variation in the measured phase offset. Removing this systematic uncertainty using the weighted averaging technique produces a much smaller uncertainty in the variation of the retrieved phase.

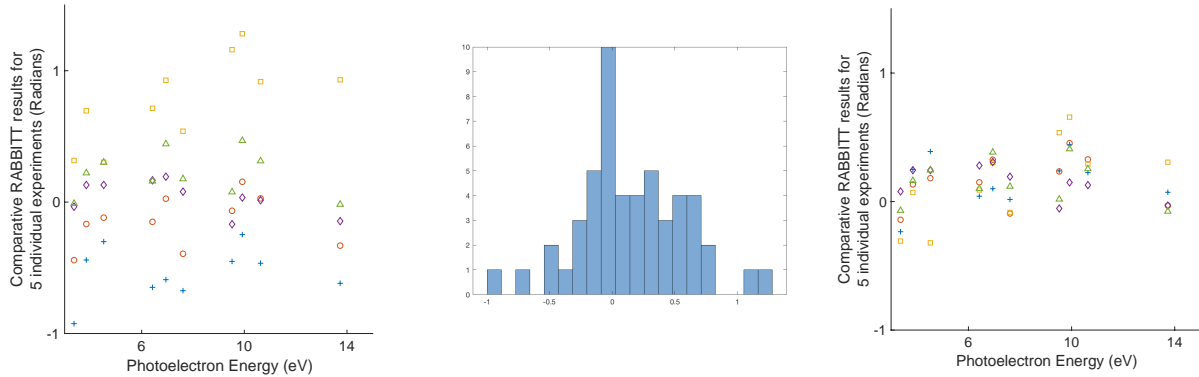


FIG. S4: a) (left): the comparative APTS results for five chronologically simultaneous experiments. These results are shown after the delay-stage drift values are compensated by interpolating drift between Kr reference measurements. It is clear that there is still a systematic error in timing overlap, given that all scans showcase similar trend lines but with different offsets. b) (middle): a histogram distribution of the averaged phase offsets measured. c) (right): The same experimental phase results as shown in figure S4a, however the average of each experiment's measured values is set to be the same value - the value determined to be the mean of the offset distribution presented in.

C. Comparative RABBITT

As described in the main paper, the extracted phase offset must be processed to isolate the phase component of interest, the photoionization phase, described in equations 2-5 of the main paper. Referencing the measured time delay to a known target gas means that:

$$\tau_2^{(I)} - \tau_2^{(\text{Kr})} = \Delta\tau_{\text{comp}}^{(I)} \approx \tau_{\text{PI}}^{(I)} - \tau_{\text{PI}}^{(\text{Kr})} + \Delta\tau_{c,c} \quad (3)$$

After applying the drift compensation procedure outlined above, we reference the extracted CO₂ two-photon photoionization time delays to those measured in krypton. The referenced time-delays ($\Delta\tau_{\text{comp}}^{(I)}$) are shown in Figure S5. To produce the data shown in Fig 1, panels (a), we add the theoretical value of the photoionization time delay in krypton[?] to the X -state measurements. For panel (b), we take the difference between the A and B -state delays. This is done to minimize the separation of ionization thresholds for the signals being compared. Existing models for calculating $\Delta\tau_{c,c}$ lose accuracy at low photoelectron energies. The inaccuracy can be sidestepped by minimizing the change in energy across which $\Delta\tau_{c,c}$ is

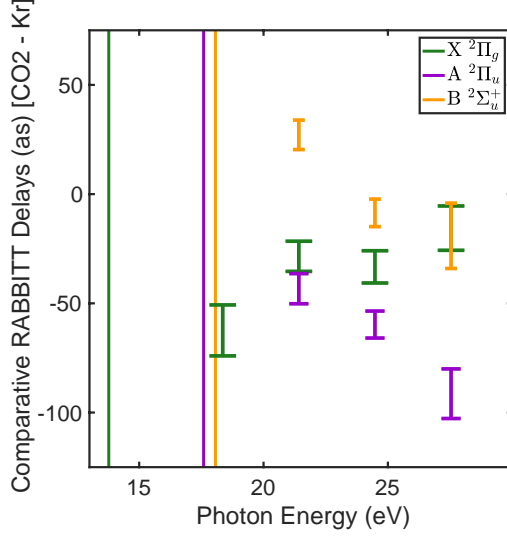


FIG. S5: The comparative RABBITT findings for this work, as expressed in eqn. 3. The vertical lines on the left side of the plot present the ionization thresholds for each of the three cationic states presented. The errorbars represent 2σ uncertainty. Not shown is a systematic error of $2\sigma = 26.2$ as associated with delay stage drift compensation. This delay-stage error is a universal error value for all data points and can be thought of as an error in assigning the location of $\tau = 0$ on the axis.

calculated. Results presented in the main paper use the $(P + A)'$ model [1]. The $B - A$ data point near photon energy $\hbar\omega = 21.4$ eV was dropped because of $\Delta\tau_{c.c}$ model uncertainty.

III. THEORY

A. Channel Coupling in Two-Color Photoionization

The interferometric ionization technique used in this work measures the delay in two-color photoionization defined as [1, 2]:

$$\tau_n(2q, \hat{k}, \hat{R}) = \frac{1}{2\omega} \text{Arg} \left[M_n^{(2)*}(\vec{k}; \epsilon_0 + \Omega_{2q+1}, \hat{R}) M_n^{(2)}(\vec{k}; \epsilon_0 + \Omega_{2q-1}, \hat{R}) \right], \quad (4)$$

where, \vec{k} is the final momentum of the outgoing electron for ionic channel n , \hat{R} defines the orientation of the molecular axis relative to the laser polarization, and $\hbar\Omega_{2q\pm 1}$ are the energies of the XUV photons which interfere to create the $2q^{\text{th}}$ sideband. We assume that $\hbar\Omega_{2q\pm 1}$ is larger than any of the relevant channel binding energies. The two-photon ionization matrix

element ($M_n^{(2)}$) for channel n is given by:

$$M_n^{(2)}(\vec{k}; \epsilon_0 + \Omega, \hat{R}) = -iE_\omega E_X \sum_p \int d\epsilon_i \frac{\langle \Psi_{\vec{k},n}^{(-)} | \vec{\mu}_\omega \cdot \vec{r} | \Psi_{i,p} \rangle \langle \Psi_{i,p} | \vec{\mu}_X \cdot \vec{r} | \Psi_0 \rangle}{\epsilon_0 + \hbar\Omega - \epsilon_i}, \quad (5)$$

where $\Psi_{\vec{k},n}^{(-)}$ is the observed final state wavefunction of momentum \vec{k} in ionic channel n , and $\Psi_{i,p}$ is the intermediate state of energy ϵ_i in ionic channel p produced by XUV ionization of the ground state, Ψ_0 with negative energy ϵ_0 . In Eqn. 5 we have ignored the far off-resonance matrix element, where the IR pulse interacts before XUV pulse. Thus, Eqn. 4 is both emission angle- and orientation-resolved. Recently Douguet *et al.* developed a full numerical theory to describe $M_n^{(2)}$ using the complex Kohn variational method [3]. Here we develop an intermediate theory, similar to that originally developed by Dahlstrom *et al.* [4], which focuses on the long-range behavior of the wavefunction. For simplicity, we assume that both the XUV and IR fields are co-polarized and linear. Our approach for analyzing Eqn. 5 is to express the scattering wavefunctions using a close coupling expansion

$$|\Psi_{\vec{k},n}^{(-)}\rangle = \sum_p \int d^3\vec{r} F_{p,n\vec{k}}(\vec{r}) a^\dagger(\vec{r}) |\Phi_p\rangle \quad (6)$$

in which Φ_p are the (N-1)-electron wavefunctions for the residual ion in channel p , $a^\dagger(\vec{r})$ is the creation operator for a (properly spin-coupled) electron at position \vec{r} , and $F_{p,n\vec{k}}$ is a single electron wavefunction. The sum over cation channels p in Eqn. 6 is complete, but the asymptotic form of the wavefunction concerns only the channels p, n for which photoionization is allowed. The asymptotic form of the single-electron wavefunctions $F_{p,n}$ for open channels is encoded by the S-matrix,

$$F_{p,n\vec{k}}(\vec{r}) \xrightarrow{r \rightarrow \infty} \sum_{\substack{LM \\ lm}} Y_l^m(\hat{k}) \left[h_{lm}^{(+)}(\vec{r}) \delta_{LM}^{np} + h_{lm}^{(-)}(\vec{r}) S_{LM}^{*np}(k) \right] \quad (7)$$

where Y_L^M are the spherical harmonic functions, and we have defined the regular-incoming ($h^{(+)}$) and irregular-outgoing ($h^{(-)}$) Coulomb waves as,

$$\begin{aligned} h_{LM}^{(+)} &= \frac{1}{\sqrt{2}} \left(f_{LM}^{nk} + i g_{LM}^{nk} \right) & f_{LM}^{nk} &\xrightarrow{r \rightarrow \infty} \frac{N_k}{r} \sin[kr + \Theta_{kL}(r)] Y_L^M(\hat{r}) \\ h_{LM}^{(-)} &= \frac{1}{\sqrt{2}} \left(f_{LM}^{nk} - i g_{LM}^{nk} \right) & g_{LM}^{nk} &\xrightarrow{r \rightarrow \infty} \frac{N_k}{r} \cos[kr + \Theta_{kL}(r)] Y_L^M(\hat{r}). \end{aligned} \quad (8)$$

f and g are the regular and irregular Coulomb function respectively, and $N_k = \sqrt{2/\pi k}$ is a normalization constant. The phase of the Coulomb functions is given by,

$$\Theta_{kL}(r) = \frac{1}{k} \ln(2kr) - \frac{L\pi}{2} + \sigma_L, \quad (9)$$

where $\sigma_L = \arg[\Gamma(L + 1 - i/k)]$ is the scattering phase shift induced by the Coulomb-potential, and Γ is the complex gamma function.

Using Eqns. 6 and 7 we can rewrite the matrix element between the intermediate and final states, $\langle \Psi_{\vec{k},n}^{(-)} | \vec{r} | \Psi_{i,p} \rangle$,

$$\begin{aligned} \langle \Psi_{\vec{k},n}^{(-)} | \vec{r} | \Psi_{i,p} \rangle &= \sum_{qq'} \langle \Phi_q F_{q,nk} | \vec{r} | \Phi_{q'} F_{q',p\kappa} \rangle \\ &= \sum_{qq'} \langle \Phi_q | \vec{r} | \Phi_{q'} \rangle \langle F_{q,nk} | F_{q',p\kappa} \rangle + \delta_{qq'} \langle F_{q,nk} | \vec{r} | F_{q',p\kappa} \rangle \\ &= \sum_q \langle F_{q,nk} | \vec{r} | F_{q,p\kappa} \rangle, \end{aligned} \quad (10)$$

where we have assumed that there are no resonant transitions between the residual ionic states. Following the approach laid out by Dahlstrom *et al.* we rewrite Eqn. 5 using Eqn. 6,

$$M_n^{(2)}(\vec{k}; \epsilon_0 + \Omega, \hat{R}) = \frac{1}{i} \sqrt{\frac{4\pi}{3}} E_\omega E_X D_{00}^{(1)}(\hat{R}) D_{00}^{(1)}(\hat{R}) \sum_q \langle F_{q,nk} | r Y_1^0(\hat{r}) | \rho_{q,\kappa} \rangle, \quad (11)$$

where $D_{lk}^{(j)}(\hat{R})$ is the Wigner matrix which rotates the polarization of the XUV and IR pulses into the molecular frame, and we have defined the first-order perturbed wavefunction for the q^{th} channel, $\rho_{q,\kappa}(r)$ as

$$\rho_{q,\kappa} = \sum_p \int d\epsilon_\kappa d\hat{\Omega}_{\hat{\kappa}} \frac{F_{q,p\kappa}(\vec{r}) \langle \psi_{\vec{k},p}^{(-)} | z | \Phi_0 \rangle}{\epsilon_0 + \hbar\Omega - \epsilon_\kappa}$$

Using Eqn. 7 as an equality we rewrite $\rho_{q,\kappa}$,

$$\begin{aligned} \rho_{q,\kappa} &= \sum_p \sum_{\substack{LM \\ lm}} \int d\hat{\Omega}_{\hat{\kappa}} Y_L^M(\hat{\kappa}) \left[\int d\epsilon_\kappa \delta_{\substack{qp \\ LM \\ lm}} \frac{h_{p\kappa}^{(+)}(\vec{r}) \langle \psi_{\vec{k},p}^{(-)} | z | \Phi_0 \rangle}{\epsilon_0 + \hbar\Omega - \epsilon_\kappa} \right. \\ &\quad \left. + \int d\epsilon_\kappa S_{\substack{qp \\ LM \\ lm}}^*(\kappa) \frac{h_{p\kappa}^{(-)}(\vec{r}) \langle \psi_{\vec{k},p}^{(-)} | z | \Phi_0 \rangle}{\epsilon_0 + \hbar\Omega - \epsilon_\kappa} \right] \end{aligned} \quad (12)$$

We rewrite the asymptotic form on Eqn. 12 using the following relations from Ref. [1]

$$\begin{aligned} \int d\epsilon_\kappa \frac{f_{LM}^{p\kappa} \langle \psi_{\vec{k},p}^{(-)} | z | \Phi_0 \rangle}{\epsilon_0 + \hbar\Omega - \epsilon_\kappa} &= -\frac{\pi N_\kappa}{r} Y_L^M(\hat{r}) \exp \left[i\kappa r + i\Theta_{\kappa L}(r) \right] \langle \psi_{\vec{k},p}^{(-)} | z | \Phi_0 \rangle \\ \int d\epsilon_\kappa \frac{g_{LM}^{p\kappa} \langle \psi_{\vec{k},p}^{(-)} | z | \Phi_0 \rangle}{\epsilon_0 + \hbar\Omega - \epsilon_\kappa} &= -i \frac{\pi N_\kappa}{r} Y_L^M(\hat{r}) \exp \left[i\kappa r + i\Theta_{\kappa L}(r) \right] \langle \psi_{\vec{k},p}^{(-)} | z | \Phi_0 \rangle \end{aligned}$$

Then $\rho_{q,\kappa}$ becomes

$$\rho_{q,\kappa} = -\frac{\pi N_\kappa}{r} \sum_p \sum_{\substack{LM \\ lm}} Y_l^m(\hat{r}) S_{\substack{pq \\ LM \\ lm}}^*(\kappa) \exp[i\kappa r + i\Theta_{\kappa l}(r)] I_{p,lm}(\kappa) \quad (13)$$

where

$$I_{p,lm}(\kappa) = \int d\hat{\Omega}_{\hat{\kappa}} Y_l^m(\hat{\kappa}) \left\langle \psi_{\hat{\kappa},p}^{(-)} \middle| z \middle| \Phi_0 \right\rangle \quad (14)$$

is the partial wave expansion of the XUV dipole matrix element for ionization to the p channel, which is calculated using the complex Kohn approach, and described in the next section.

Next we must evaluate the matrix element, $\langle F_{q,nk} | r | \rho_{q,p\kappa} \rangle$

$$\begin{aligned} \langle F_{q,nk} | r Y_1^0 | \rho_{q\kappa} \rangle &= -\pi N_k N_\kappa \sum_p \sum_{\substack{LM \\ L'M'}} Y_L^M(\hat{k}) \sum_{\substack{lm \\ l'm'}} \left\langle Y_l^m | Y_1^0 | Y_{l'}^{m'} \right\rangle I_{p,l'm'}(\kappa) \\ &\times \left[S_{\substack{pq \\ L'M' \\ l'm'}}^*(\kappa) \delta_{\substack{nq \\ LM \\ lm}} \int_0^\infty dr \exp[i(\kappa - k)r] r \exp[i(\Theta_\kappa(r) - \Theta_k(r))] \right. \\ &\left. + S_{\substack{pq \\ L'M' \\ l'm'}}^*(\kappa) S_{\substack{qn \\ LM \\ lm}}(k) \int_0^\infty dr \exp[i(\kappa + k)r] r \exp[i(\Theta_\kappa(r) + \Theta_k(r))] \right] \quad (15) \end{aligned}$$

We define the following integrals,

$$J_\pm(\kappa, k) = \pm \frac{1}{2i} \int_0^\infty dr r^{1+i(1/\kappa \pm 1/k)} \exp[i(\kappa \pm k)r]$$

and rewrite Eqn. 15,

$$\begin{aligned} \langle F_{q,nk} | r | \rho_{q\kappa} \rangle &\sim -\pi N_\kappa N_k \sum_p \sum_{\substack{LM \\ L'M'}} Y_L^M(\hat{k}) \sum_{\substack{lm \\ l'm'}} \left\langle Y_l^m | Y_1^0 | Y_{l'}^{m'} \right\rangle I_{p,l'm'}(\kappa) \\ &\times S_{\substack{pq \\ L'M' \\ l'm'}}^*(\kappa) \left(\delta_{\substack{nq \\ LM \\ lm}} J_- + S_{\substack{qn \\ LM \\ lm}}(k) J_+ \right) \quad (16) \end{aligned}$$

As described in Ref. [1], the contribution from the J_+ integral is much smaller than that of the J_- integral. This is because of the IR photon energy is small compared to the final electron energy, and thus $k^2/2 - \kappa^2/2 = \omega < k^2/2$. Therefore the difference $|\kappa - k|$ is much smaller than the sum $\kappa + k$ and the fast oscillations of $\exp[i(\kappa + k)r]$ in the J_+ integral lead to a cancellation. Thus we arrive at the expression,

$$\langle F_{q,nk} | r | \rho_{q\kappa} \rangle = -\pi N_k N_\kappa \sum_p \sum_{\substack{LM \\ L'M' \\ l'm'}} Y_L^M(\hat{k}) I_{p,l'm'}(\kappa) \left\langle Y_L^M | Y_1^0 | Y_{l'}^{m'} \right\rangle S_{\substack{pq \\ L'M' \\ l'm'}}^*(\kappa) \delta_{nq} J_-(\kappa, k). \quad (17)$$

Using Eqn. 17 we arrive at the following simplification for Eqn. 5

$$M_n^{(2)}(\vec{k}; \epsilon_0 + \Omega, \hat{R}) = \frac{4\pi^2}{3i} E_\omega E_X D_{00}^{(1)}(\hat{R}) D_{00}^{(1)}(\hat{R}) N_k N_\kappa \sum_p \sum_{\substack{LM \\ L'M'}} Y_L^M(\hat{k}) \quad (18)$$

$$\times \sum_{l'm'} I_{p,l'm'}(\kappa) \left\langle Y_L^M | Y_1^0 | Y_{l'}^{m'} \right\rangle S_{L'M'}^{*pn}(\kappa) J_-(\kappa, k).$$

This can be recast in the same form as the expression derived by Baykusheva and Worner [2]:

$$M_n^{(2)}(\vec{k}; \epsilon_0 + \Omega, \hat{R}) = N_k N_\kappa J_-(k, \kappa) \sum_{LM} b_{n,LM}(\kappa; \hat{R}) Y_L^M(\hat{k}) \quad (19)$$

But now $b_{n,LM}$ is defined as,

$$b_{n,LM}(\kappa; \hat{R}) = \frac{4\pi}{3i} E_\omega E_X D_{00}^{(1)}(\hat{R}) D_{00}^{(1)}(\hat{R}) \sum_p \sum_{\substack{L'M' \\ l'm'}} I_{p,l'm'}(\kappa) \left\langle Y_L^M | Y_1^0 | Y_{l'}^{m'} \right\rangle S_{L'M'}^{*pn}(\kappa) \quad (20)$$

The angle- and orientation-dependent delay in Eqn. 4 is then given by

$$\tau_n(2q, \hat{k}, \hat{R}) = \frac{1}{2\omega} \text{Arg} [N_{k-\omega} J_-(k, k-\omega) N_{k+\omega}^* J_-^*(k, k+\omega)] \quad (21)$$

$$+ \frac{1}{2\omega} \text{Arg} \left[\sum_{\substack{LM \\ L'M'}} Y_L^{M*}(\hat{k}) Y_{L'}^{M'}(\hat{k}) b_{n,LM}^*(k-\omega; \hat{R}) b_{n,L'M'}(k+\omega; \hat{R}) \right]$$

$$= \tau_{cc}(k) + \tau_{PI}(2q, \hat{k}, \hat{R})$$

As pointed out in Ref. [2], the first term in Eqn. 21 only depends on the photon energy and can be interpreted as a continuum-continuum delay (τ_{cc}). The second term in Eqn. 21 is again a target-specific delay (τ_{PI}), but the single photon delays are modified by the interaction with the IR light. In addition to this modification, described by Baykusheva and Worner, Eqn. 20 shows that the channel coupling adds additional modifications. In the absence of any channel coupling, the S -matrix is purely diagonal, Eqn. 20 reduces to the expression derived by Baykusheva and Worner.

B. Complex Kohn Photoionization Calculations

In this section we describe how we calculate the single-photon, channel-resolved dipole matrix element (Eqn. 11 of the main text),

$$d_n(\vec{k}) = \sum_{LM} Y_L^M(\hat{k}) I_{n,LM}(k), \quad (22)$$

State	Ground neutral	$X \ ^2\Pi_g$	$A \ ^2\Pi_u$	$B \ ^2\Sigma_u$	$C \ ^2\Sigma_g$
Energy	-187.654	-187.150	-186.964	-186.947	-186.894
IP	0.504	0.690	0.707	0.760	
IP (eV)	13.703	18.774	19.232	20.677	
IP (lit.)	13.669				

TABLE I: Energies (in hartree or eV) of the ground and cation electronic states obtained from this calculation at $R=2.140$ compared with benchmark aug-pvtz coupled cluster results [Can't immediately find higher IPs. NIST CCCBDB has CO2 vertical IP = 13.669eV using aug-cc-pVTZ, CCSD(T). <https://cccbdb.nist.gov/ie2x.asp?casno=124389>]

described in Eqn. 14. As described in the main text, the channel-resolved dipole matrix element is computed using the complex Kohn method for photoionization [5–23], using representations of the initial neutral state and of the final cation states obtained with one single 11-orbital basis. The orbital basis was obtained using the *Columbus* quantum chemistry program [24–28]. The orbitals are obtained by minimizing a weighted sum of energies of the closed-shell Hartree-Fock ground state neutral and six microstates of the cation, corresponding to the $X \ ^2\Pi_g$, $A \ ^2\Pi_u$, $B \ ^2\Sigma_u$, and $C \ ^2\Sigma_g$ electronic states, at bond distance $R = 2.140a_0$. The relative weights for ground and cation are 6:1:1:1:1:1, such that the orbitals obtained are a balanced compromise between those optimized for the neutral and cation. The energies of these states are listed in Table I. The primitive basis for this MCSCF calculation was Dunning's *aug-cc-pVDZ* basis set [29], comprising 75 basis functions, with 35 additional basis functions on the carbon atom (at the origin) that are listed in Table II. For the complex Kohn scattering calculation, the $L = 0, 1, 2, 3$ partial wave scattering channels are used,

$$\left| \Psi_{\vec{k},n}^{(-)} \right\rangle = \sum_{LM} Y_L^M(\hat{k}) \left| \psi_{kLM,n}^{(-)} \right\rangle \quad (23)$$

Eleven linear combinations of the 110 Gaussian basis functions are obtained by the state-averaged MCSCF calculation, and the orthogonal complement of 99 basis functions are used along with numerical continuum functions with $L = 0, 1, 2, 3$ to construct the scattering wave functions $\psi_{kLM,n}^{(-)}$, which is described by Eqn. 6. The dipole matrix element between the scattering wavefunction and the initial state wavefunction is calculated within the approximation of separable exchange [5, 6, 10]. Two different complex Kohn calculations are

Partial wave	Exponents				Number of functions
s	0.0200	0.0080	0.0030	0.0012	4
p	0.0180	0.0080	0.0035		9
d	0.0750	0.0320			12
f	0.2500				10
all					35

TABLE II: Extra basis functions used in the Kohn calculation, those besides Dunning’s aug-cc-pVDZ basis [29].

performed, one in which the four electronic state channels are uncoupled from one another, and one in which they are fully coupled, in the construction of $|\psi^{(-)}\rangle$. The dipole matrix element is expanded in a partial wave basis as described in Eqn. 22

C. Molecular Photoionization Delays

The partial wave decomposition of the single-photon dipole matrix element, $I_{n,LM}(k)$ is calculated as described in the previous section. The results are used to calculate $b_{LM}(k; \hat{R})$ described in Eqn. 20. For the calculation presented in the main text and below, we make the assumption that the S -matrix in Eqn. 20 is purely diagonal. In this approximation, we fully include channel coupling in the single-photon ionization process, but neglect the effect of the channel coupling in the interaction with the IR-photon. The result is the emission angle (\hat{k})- and orientation angle (\hat{R})-resolved photoionization delays for a central photon energy of $\hbar\Omega_{2q}$. The molecular frame (MF) photoionization delays are shown in figures S6 and S7. The delays are calculated in the two limiting cases where the XUV (and IR) polarization is aligned along the molecular axis (Figures S6a and S7a), and when this polarization is perpendicular to the molecular axis (Figures S6b and S7b). We show the results of both the single channel (Figure S6) and coupled-channel (Figure S7) calculations.

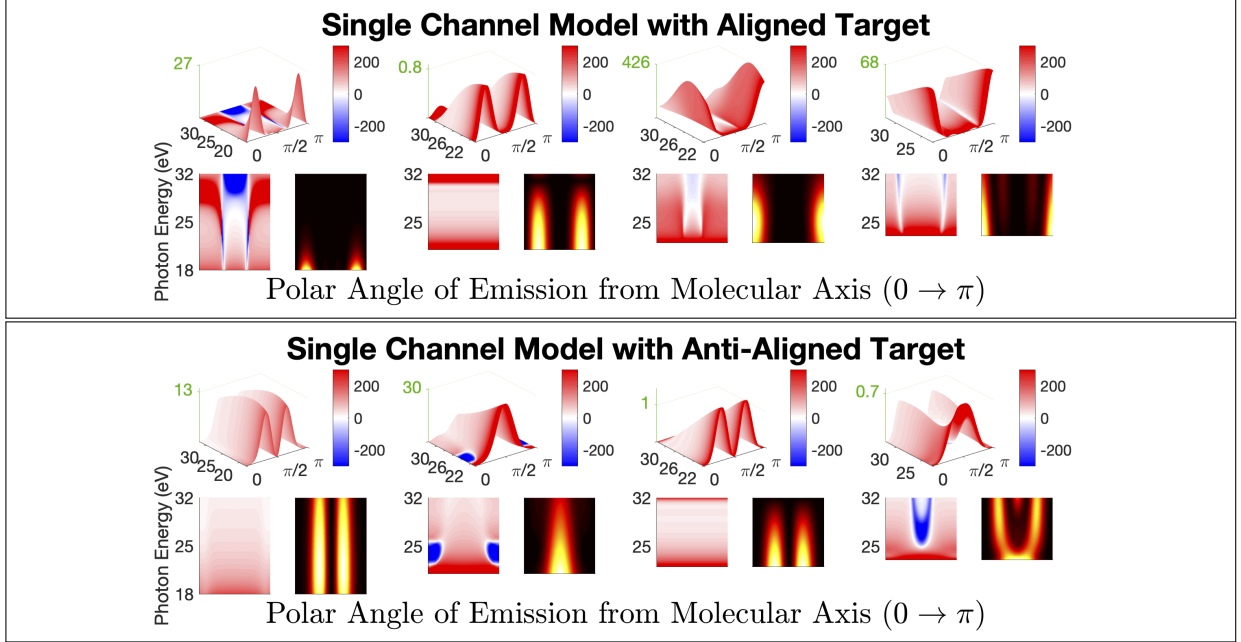


FIG. S6: Calculated molecular frame two-photon photoionization time delays, $\tau_{PI}(2q, \hat{k}, \hat{R})$, for different molecular orientations. In each box, the upper row of plots shows polar surfaces, as a function of photon energy and photoelectron emission angle, where the topography is defined by the photoionization cross section and colormap by the photoionization delay time. Below each contour plot, we show the calculated photoionization time delay on the left and calculated cross section on the right. Moving across each row, we show the results for ionization in the $X^2\Pi_g$, $A^2\Pi_u$, $B^2\Sigma_u$, and $C^2\Sigma_g$ cationic channels. The green number along the z-axis of the surface plot provides context for the relative cross sections of this particular channel. We show results for single channel calculations, where channel coupling is neglected, for the case when both the XUV and IR polarizations are linear and either aligned with the molecular axis (Aligned target) or perpendicular to the molecular axis (Anti-Aligned Target).

D. Effects of Angular Averaging

There are a number of interesting features in the MF, angle-resolved photoemission delays, however, our experiments use a randomly oriented target gas and magnetic bottle electron time of flight spectrometer which does not resolve emission angle. Therefore Eqn. 21 needs to be averaged over both the molecular axis distribution or the outgoing electron angle. The contributions from each pair of (\hat{k}, \hat{R}) are incoherently averaged, weighed by a cross section

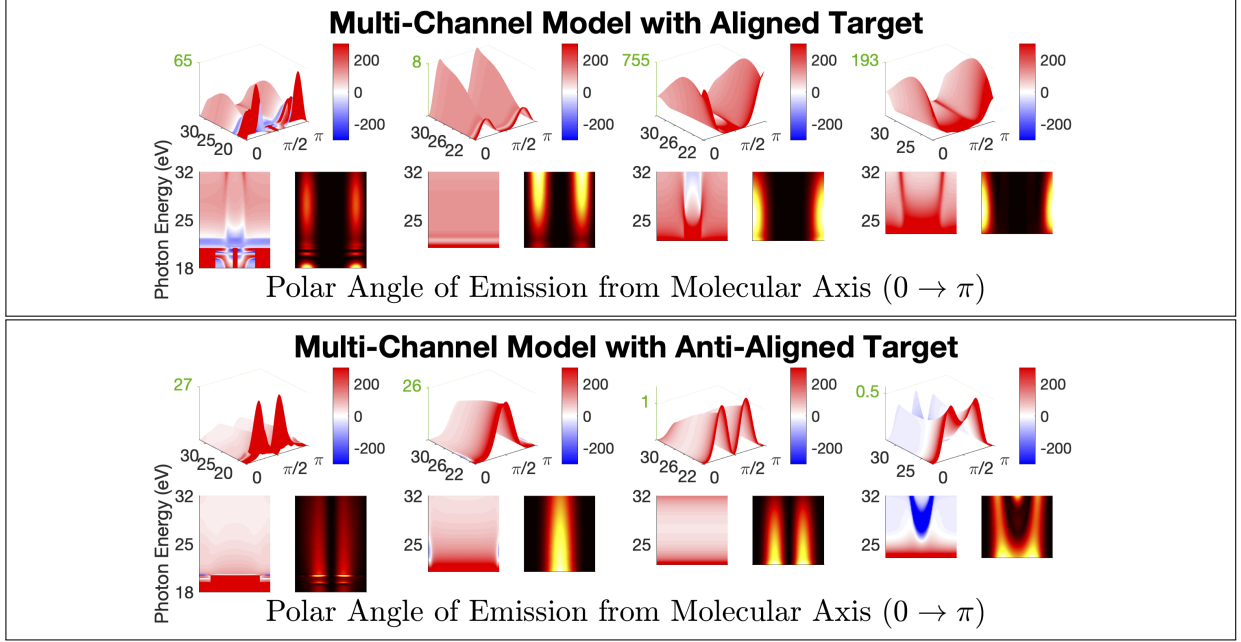


FIG. S7: Calculated molecular frame two-photon photoionization time delays, $\tau_{PI}(2q, \hat{k}, \hat{R})$, for different molecular orientations. In each box, the upper row of plots shows polar surfaces, as a function of photon energy and photoelectron emission angle, where the topography is defined by the photoionization cross section and colormap by the photoionization delay time. Below each contour plot, we show the calculated photoionization time delay on the left and calculated cross section on the right. Moving across each row, we show the results for ionization in the $X^2\Pi_g$, $A^2\Pi_u$, $B^2\Sigma_u$, and $C^2\Sigma_g$ cationic channels. The green number along the z-axis of the surface plot provides context for the relative cross sections of this particular channel. We show results for the coupled-channel calculation described above, for the case when both the XUV and IR polarizations are linear and either aligned with the molecular axis (Aligned target) or perpendicular to the molecular axis (Anti-Aligned Target).

term $|b_{n,LM}^*(k - \omega; \hat{R})b_{n,L'M'}(k + \omega; \hat{R})|$. The measured photoionization time delays are then compared to the calculated average,

$$\tau_{PI}(2q) = \frac{1}{2\omega} \text{Arg} \left[\int d\hat{\Omega}_{\hat{R}} \int d\hat{\Omega}_{\hat{k}} \sum_{\substack{LM \\ L'M'}} Y_L^{M*}(\hat{k}) Y_{L'}^{M'}(\hat{k}) b_{n,LM}^*(k - \omega; \hat{R}) b_{n,L'M'}(k + \omega; \hat{R}) \right]. \quad (24)$$

Eqn. 24 is an averaged quantity that is compared to the experimental measurements in

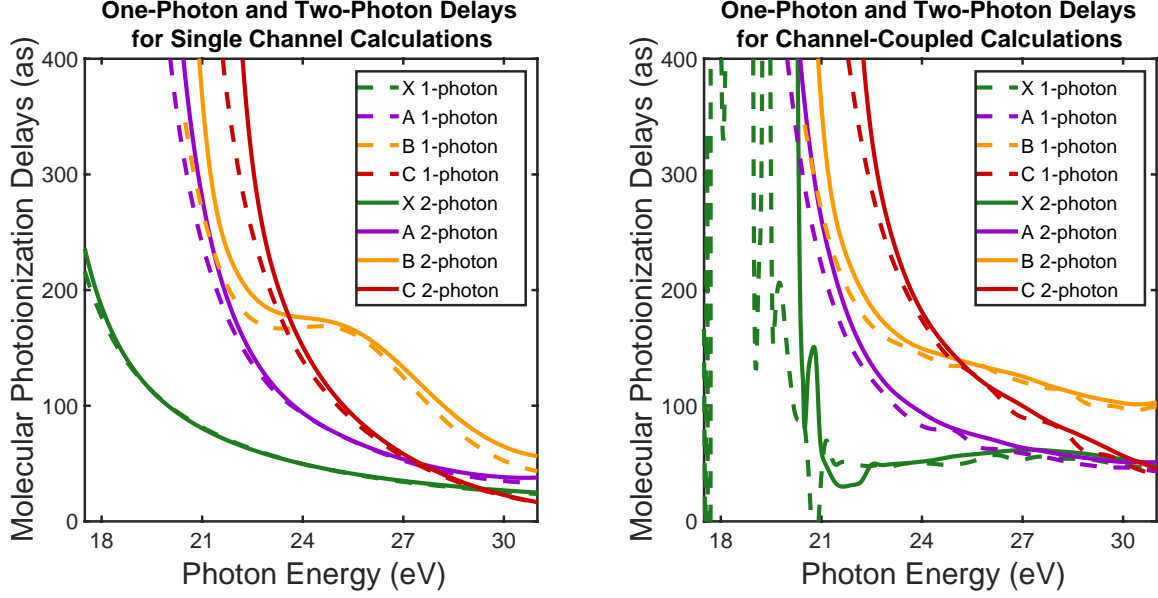


FIG. S8: Comparison of angle-averaged single-photon and angle-averaged two-photon photoionization delay values for the single channel (left) and coupled-channel (right) results. Most features are consistent between τ_1 and $\tau_{P.I.}$. There is difference in the low-energy region for the X state results. The Rydberg series consists of very long delays at discrete energies for the single-photon values, which get smeared into a plateau for the two-photon calculation.

Figure 1 of the main text. We can perform similar averaging for the single-photon photoionization delay, $\tau_1(E, \hat{k}, \hat{R})$, defined in Eqn. 9 of the main text. In Figure S8 we compare the emission angle- and orientation-averaged single-photon ($\tau_1(E)$) and two-photon ($\tau_{PI}(2q)$) delay, and show that the two values are nearly identical. This is in stark contrast to the previous work by Baykusheva and Wornor, where it was observed that for the N_2O target, there were substantial difference between the two values [2]. This is likely due to difference in the molecular system, such as the presence of inversion symmetry in the CO_2 system, which should simplify the partial wave expansion of the photoionized EWP, and lessen the effects that IR induced angular momentum coupling has on the emission angle-averaged photoionization delay times.

-
- [1] J. M. Dahlström, D. Guénot, K. Klünder, M. Gisselbrecht, J. Mauritsson, A. L’Huillier, A. Maquet, and R. Taïeb, Theory of attosecond delays in laser-assisted photoionization, *Chemical Physics* **414**, 53 (2013).
- [2] D. Baykusheva and H. J. Wörner, Theory of attosecond delays in molecular photoionization, *The Journal of Chemical Physics* **146**, 124306 (2017).
- [3] N. Douguet, B. I. Schneider, and L. Argenti, Application of the complex Kohn variational method to attosecond spectroscopy, *Physical Review A* **98**, 023403 (2018).
- [4] J. M. Dahlström, A. L’Huillier, and A. Maquet, Introduction to attosecond delays in photoionization, *Journal of Physics B: Atomic, Molecular and Optical Physics* **45**, 183001 (2012).
- [5] T. N. Rescigno and A. E. Orel, Separable approximation for exchange interactions in electron-molecule scattering, *Physical Review A* **24**, 1267 (1981).
- [6] T. N. Rescigno and B. I. Schneider, Disappearance of continuum exchange integrals from algebraic variational calculations of electron scattering, *Physical Review A* **37**, 1044(R) (1988).
- [7] B. I. Schneider and T. N. Rescigno, Complex Kohn variational method: Application to low-energy electron-molecule collisions, *Physical Review A* **37**, 3749 (1988).
- [8] A. E. Orel and T. N. Rescigno, Variational expressions for first-order properties involving continuum wave functions, *Physical Review A* **41**, 1695 (1990).
- [9] T. N. Rescigno and A. E. Orel, Continuum basis functions in the complex Kohn variational method, *Physical Review A* **43**, 1625 (1991).
- [10] C. W. McCurdy and T. N. Rescigno, Beyond the primitive separable exchange approximation in electron-molecule scattering, *Physical Review A* **46**, 255 (1992).
- [11] T. N. Rescigno, A. E. Orel, and C. W. McCurdy, Algebraic variational approach to atomic and molecular photoionization cross sections: Removing the energy dependence from the basis, *Physical Review A* **55**, 342 (1997).
- [12] T. N. Rescigno and C. W. McCurdy, Improvements to the “standard” complex Kohn variational method: Towards the development of an “R-matrix theory without a box”, in *Novel Aspects of Electron-Molecule Collisions*, edited by K. H. Becker (World Scientific Publishing, Singapore, 1998) 325.
- [13] C. W. McCurdy, T. N. Rescigno, W. A. Isaacs, and D. E. Manolopoulos, Calculation of

- scattering amplitudes as continuous functions of energy: R-matrix theory without a box, *Physical Review A* **57**, 3511 (1998).
- [14] T. N. Rescigno, B. H. Lengsfeld, and A. E. Orel, Interchannel coupling and ground state correlation effects in the photoionization of CO, *The Journal of Chemical Physics* **99**, 5097 (1993).
- [15] A. E. Orel and T. N. Rescigno, Photoionization of ammonia, *Chemical Physics Letters* **269**, 222 (1997).
- [16] S. Miyabe, C. W. McCurdy, A. E. Orel, and T. N. Rescigno, Theoretical study of asymmetric molecular-frame photoelectron angular distributions for C 1s photoejection from CO₂, *Physical Review A* **79**, 053401 (2009).
- [17] H. Sann, T. Jahnke, T. Havermeier, K. Kreidi, C. Stuck, M. Meckel, M. S. Schöffler, N. Neumann, R. Wallauer, S. Voss, A. Czasch, O. Jagutzki, Th. Weber, H. Schmidt-Böcking, S. Miyabe, D. J. Haxton, A.E. Orel, T. N. Rescigno, and R. Dörner, Electron diffraction self-imaging of molecular fragmentation in two-step double ionization of water, *Physical Review Letters* **106**, 133001 (2011).
- [18] J. B. Williams, C. S. Trevisan, M. S. Schöffler, T. Jahnke, I. Bocharova, H. Kim, B. Ulrich, R. Wallauer, F. Sturm, T. N. Rescigno, A. Belkacem, R. Dörner, Th. Weber, C. W. McCurdy, and A. L. Landers, Imaging polyatomic molecules in three dimensions using molecular frame photoelectron angular distributions, *Physical Review Letters* **108**, 233002 (2012).
- [19] N. Douguet, T. N. Rescigno, and A. E. Orel, Time-resolved molecular-frame photoelectron angular distributions: Snapshots of acetylene-vinylidene cationic isomerization, *Physical Review A* **86**, 013425 (2012).
- [20] S. Marggi Poullain, C. Elkharrat, W. B. Li, K. Veyrinas, J. C. Houver, C. Cornaggia, T. N. Rescigno, R. R. Lucchese, and D. Dowek, Recoil frame photoemission in multiphoton ionization of small polyatomic molecules: photodynamics of NO₂ probed by 400 nm fs pulses, *Journal of Physics B: Atomic, Molecular and Optical Physics* **47**, 124024 (2014).
- [21] S. Fonseca dos Santos, N. Douguet, A. E. Orel, and T. N. Rescigno, Ligand effects in carbon-*K*-shell photoionization, *Physical Review A* **91**, 023408 (2015).
- [22] C. W. McCurdy, T. N. Rescigno, C. S. Trevisan, R. R. Lucchese, B. Gaire, A. Menssen, M. S. Schöffler, A. Gatton, J. Neff, P. M. Stammer, J. Rist, S. Eckart, B. Berry, T. Severt, J. Sartor, A. Moradmand, T. Jahnke, A. L. Landers, J. B. Williams, I. Ben-Itzhak, R. Dörner, A.

- Belkacem, and Th. Weber, Unambiguous observation of F-atom core-hole localization in CF₄ through body-frame photoelectron angular distributions, *Physical Review A* **95**, 011401(R) (2017).
- [23] E. G. Champenois, L. Greenman, N. Shivaram, J. P. Cryan, K. A. Larsen, T. N. Rescigno, C. W. McCurdy, A. Belkacem, and D. S. Slaughter, Ultrafast photodissociation dynamics and nonadiabatic coupling between excited electronic states of methanol probed by time-resolved photoelectron spectroscopy, *The Journal of Chemical Physics* **150**, 114301 (2019).
- [24] H. Lischka, R. Shepard, F. B. Brown, and I. Shavitt, New implementation of the graphical unitary group approach for multireference direct configuration interaction calculations, *International Journal of Quantum Chemistry* **20**, 91 (1981).
- [25] R. Shepard, I. Shavitt, R. M. Pitzer, D. C. Comeau, M. Pepper, H. Lischka, P. G. Szalay, R. Ahlrichs, F. B. Brown, and J.-G. Zhao, A progress report on the status of the *COLUMBUS* MRCI program system, *International Journal of Quantum Chemistry* **34**, 149 (1988).
- [26] H. Lischka, R. Shepard, R. M. Pitzer, I. Shavitt, M. Dallos, T. Müller, P. G. Szalay, M. Seth, G. S. Kedziora, S. Yabushita, and Z. Zhang, High-level multireference methods in the quantum-chemistry program system *COLUMBUS*: Analytic MR-CISD and MR-AQCC gradients and MR-AQCC-LRT for excited states, GUGA spin-orbit CI and parallel CI density, *Physical Chemistry Chemical Physics* **3**, 664 (2001).
- [27] H. Lischka, T. Müller, P. G. Szalay, I. Shavitt, R. M. Pitzer, and R. Shepard, *COLUMBUS*-a program system for advanced multireference theory calculations, *Wiley Interdisciplinary Reviews: Computational Molecular Science* **1**, 191 (2011).
- [28] H. Lischka, R. Shepard, I. Shavitt, R. M. Pitzer, M. Dallos, Th. Müller, P. G. Szalay, F. B. Brown, R. Ahlrichs, H. J. Böhm, A. Chang, D. C. Comeau, R. Gdanitz, H. Dachsel, C. Ehrhardt, M. Ernzerhof, P. Höchtel, S. Irlé, G. Kedziora, T. Kovar, V. Parasuk, M. J. M. Pepper, P. Scharf, H. Schiffer, M. Schindler, M. Schüler, M. Seth, E. A. Stahlberg, J.-G. Zhao, S. Yabushita, Z. Zhang, M. Barbatti, S. Matsika, M. Schuurmann, D. R. Yarkony, S. R. Brozell, E. V. Beck, , J.-P. Blaudeau, M. Ruckebauer, B. Sellner, F. Plasser, and J. J. Szymczak, *Columbus*, an ab initio electronic structure program (2012), release 7.0.
- [29] T. H. Dunning, Jr., Gaussian basis sets for use in correlated molecular calculations. I. The atoms boron through neon and hydrogen, *The Journal of Chemical Physics* **90**, 1007 (1989).